

SERDP UX-1312 FINAL REPORT

Multi-Sensor CSEM Technology for Buried Target Classification

Mark E. Everett

Department of Geology and Geophysics

Cam Nguyen

Department of Electrical and Computer Engineering

Texas A&M University
College Station, TX 77843

REPORT DOCUMENTATION PAGE					Form Approved OMB No. 0704-0188	
The public reporting burden for this collection of information is estimated to average 1 hour per response, including the time for reviewing instructions, searching existing data sources, gathering and maintaining the data needed, and completing and reviewing the collection of information. Send comments regarding this burden estimate or any other aspect of this collection of information, including suggestions for reducing the burden, to the Department of Defense, Executive Services and Communications Directorate (0704-0188). Respondents should be aware that notwithstanding any other provision of law, no person shall be subject to any penalty for failing to comply with a collection of information if it does not display a currently valid OMB control number.						
PLEASE DO NOT RETURN YOUR FORM TO THE ABOVE ORGANIZATION.						
1. REPORT DATE (DD-MM-YYYY) April 24, 2006		2. REPORT TYPE Final Report			3. DATES COVERED (From - To)	
4. TITLE AND SUBTITLE Multi-Sensor CSEM Technology for Buried Target Classification				5a. CONTRACT NUMBER		
				5b. GRANT NUMBER		
				5c. PROGRAM ELEMENT NUMBER		
6. AUTHOR(S) Everett, Mark E. Nguyen, Cam				5d. PROJECT NUMBER UX-1312		
				5e. TASK NUMBER		
				5f. WORK UNIT NUMBER		
7. PERFORMING ORGANIZATION NAME(S) AND ADDRESS(ES) Texas A&M University College Station, TX 77843					8. PERFORMING ORGANIZATION REPORT NUMBER	
9. SPONSORING/MONITORING AGENCY NAME(S) AND ADDRESS(ES) Strategic Environmental Research & Development Program Office 901 North Stuart Street, Suite 303 Arlington, VA 22203					10. SPONSOR/MONITOR'S ACRONYM(S) SERDP	
					11. SPONSOR/MONITOR'S REPORT NUMBER(S)	
12. DISTRIBUTION/AVAILABILITY STATEMENT Approved for public release; distribution is unlimited						
13. SUPPLEMENTARY NOTES						
14. ABSTRACT One of the challenges faced by geophysicists is development of improved electromagnetic induction (EMI) sensors and algorithms capable of recording target responses, isolating them from geological noise, and processing them to discriminate the nature of the target during cleanup operations. The SERDP project UX-1312 responded to this challenge. The project consisted of three tasks: sensor prototype development, software development, and integrated system test. This final report describes the accomplishments made within each task.						
15. SUBJECT TERMS UXO detection, sensors, EMI						
16. SECURITY CLASSIFICATION OF:			17. LIMITATION OF ABSTRACT N/A	18. NUMBER OF PAGES 66	19a. NAME OF RESPONSIBLE PERSON	
a. REPORT Unclassified	b. ABSTRACT Unclassified	c. THIS PAGE Unclassified			19b. TELEPHONE NUMBER (Include area code)	

This report was prepared under contract to the Department of Defense Strategic Environmental Research and Development Program (SERDP). The publication of this report does not indicate endorsement by the Department of Defense, nor should the contents be construed as reflecting the official policy or position of the Department of Defense. Reference herein to any specific commercial product, process, or service by trade name, trademark, manufacturer, or otherwise, does not necessarily constitute or imply its endorsement, recommendation, or favoring by the Department of Defense.

SERDP UX-1312 FINAL REPORT
Multi-Sensor CSEM Technology for Buried Target Classification

Mark E. Everett
Department of Geology and Geophysics

Cam Nguyen
Department of Electrical and Computer Engineering

Texas A&M University
College Station, TX 77843

Contents.

Introduction	page 1
Task 1: Sensor Prototype Development	page 1
Task 2: Software Development	page 3
Task 3: Integrated System Test	page 10
Conclusions	page 26
Publications	page 34
References	page 35

Introduction.

Unexploded ordnance (UXO) detection, discrimination and removal represents a priority environmental and geotechnical problem at U.S. military bases facing closure and realignment and in many other regions of the world including Central America, Africa, and Asia. The common factor in cleanup operations is the huge final cost per UXO removed, mainly associated with unnecessary digging operations. The probability of UXO detection on documented U.S. Army test sites can exceed 90% in carefully executed geophysical surveys; however, despite recent advances in geophysical technologies and signal processing algorithms the false alarm rates remain unacceptably high.

One of the challenges faced by geophysicists is development of improved electromagnetic induction (EMI) sensors and algorithms capable of recording target responses, isolating them from geological noise, and processing them to discriminate the nature of the target during cleanup operations. The SERDP project UX-1312 responded to this challenge. The project consists of three tasks: sensor prototype development, software development, and integrated system test. This final report describes the accomplishments made within each task.

Task 1. Sensor Prototype Development

A multi-sensor EMI system prototype has been developed. The system consists of a transmitter, a multi-channel receiver, a power supply module, a transmitting coil, multiple receiving coils, and a signal processing unit. The transmitter, receiver and

power supply constitute the system's main hardware and are completely designed on a single circuit board, thus making the system very compact and man-portable. The developed system has been demonstrated in laboratory and field for detection of UXO.

1.1 Transmitter

Figure 1 shows the transmitter block diagram, consisting basically of a pulse generator, driver and current switch. The driver is designed to produce a voltage that can alternate between a high and zero value within an appropriate time to properly control the on and off states of the current switch. The switch is turned on and off when the control voltage is set high and zero, respectively. The turn-on speed is controlled by a charging resistor and the gate-source capacitance of power MOSFET's in the switch. The turn-off duration is controlled by the time constant of the transmitter coil and the parasitic capacitances between the drain and source terminals of the power MOSFET's.

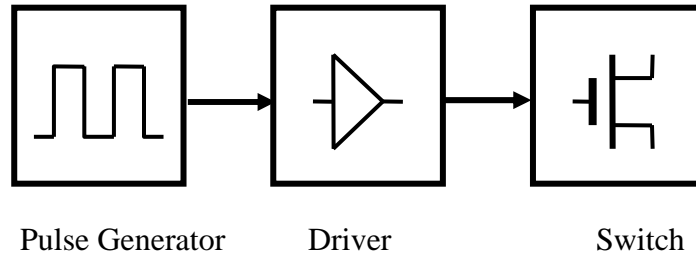


Figure 1. Transmitter block diagram.

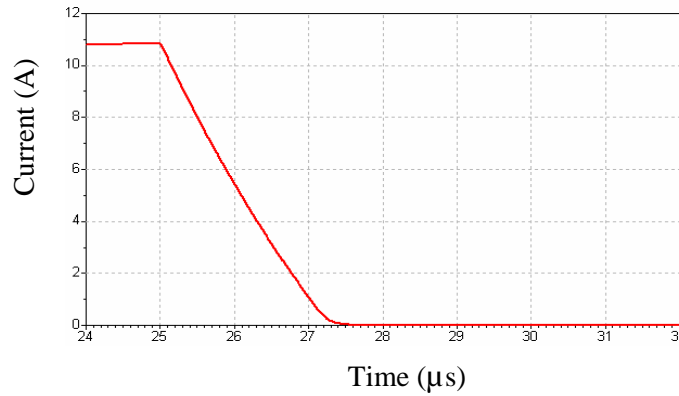


Figure 2. Transmitter calculated current.

To achieve a fast turn-off time, a damping resistor is used to reduce the time constant of the transmitter coil. Figure 2 shows the transmitter's calculated current based on a circuit simulation. The actual measured current waveform at the transmitter loop antenna, and its turn-on and turn-off behavior, is shown in Figures 3a-c. The measured results indicate a current of 10 A with a turn-off time of 2 μ s. This achieved current level and rapid turn-off is exceptional for UXO geophysics applications, since they permit the required large S/N ratio and well-defined early-time electromagnetic response. The measured decay of

the transmitter is very linear. The duty cycle and period of the current can be controlled. The rising time to reach I_{\max} is around 400 μs and is adjustable. The falling time of the current is $\sim 2 \mu\text{s}$ for 10 A.

The transmitter is realized on printed circuit board (PCB) and is therefore very lightweight and compact in size, as desired for geophysical instrumentation which must be used in potentially adverse terrain and weather conditions. As desirable for a UXO prospecting system based on EMI principles, the developed transmitter achieves simultaneously high current amplitude and fast turn-off speed.

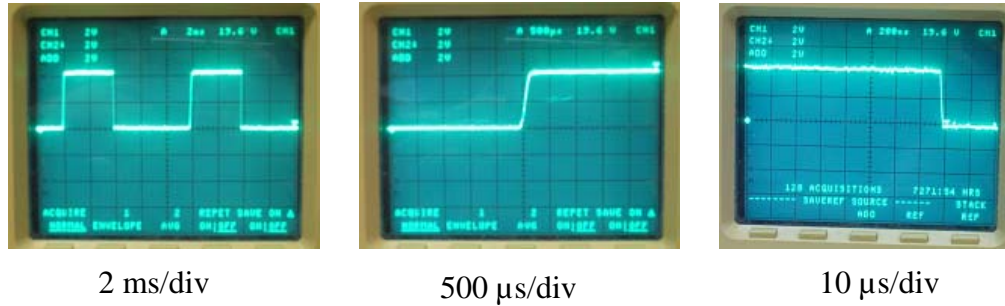


Figure 3. (a, left) Measured current in the transmitter coil. (b, middle) Current switch-on behavior. (c, right) Current shut-off behavior. The vertical scale is 5 A/div.

1.2 Receiver

The block diagram of the multi-channel receiver, shown in Figure 4, consists of a multiplexer, low-pass filter (LPF) and low-noise amplifier (LNA) connecting to multi-turn coils and a data acquisition and processing module. Nine multi-turn coils are used in the prototype version of the UX-1312 receiver, but this number is readily expandable to 16. The multiplexer is used to provide fast switching among the receiver coils.

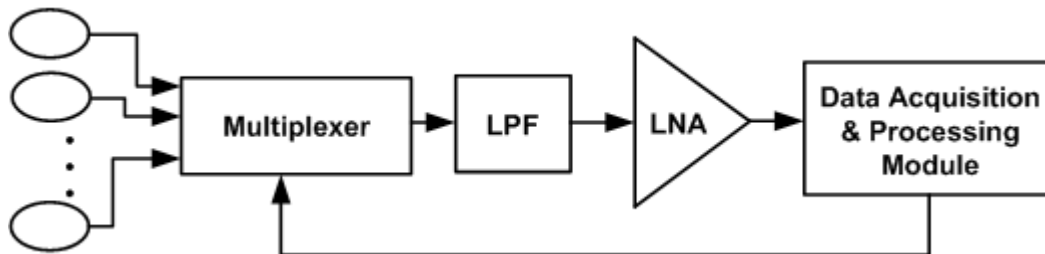


Figure 4. Receiver block diagram with multiple loop antennas.

A 16-bit data acquisition (DAQ) card is used in the data acquisition and processing module to acquire the signals associated with the EMI response of a buried UXO target.

Three-bit digital signals from the digital output of the DAQ card are sent to the inputs of the multiplexer to select the proper channel prior to the measurement. The signal from the selected channel is then sent to the common output of the multiplexer, which is then connected to the analog input of the 16-bit DAQ card through the LPF and LNA. The receiver circuit is realized using printed circuits in the same circuit board as the transmitter circuit.

Figure 5 shows a typical EMI response signal from a UXO target. The signal, originating as an induced voltage at a receiver coil, is recorded at the corresponding channel on the receiver module.

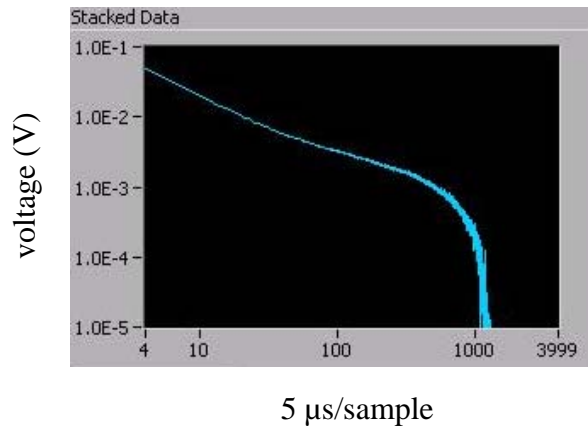


Figure 5. Typical signal received by one receiver channel measured at the receiver coil.

1.3 Transmitter and Receiver Coils

The transmit coil has three turns, a diameter of 30 cm, and inductance of approximately 8 mH. Thick copper wire is used to minimize resistive loss, thereby improving the antenna efficiency. Figure 6 shows a receive coil. It consists of multi-turn loop integrated with a ferrite annulus core. The receive coil uses magnetic copper wire and has 260 turns with 9-cm diameter. Its self resistance is 4 Ω . A 1-K Ω damping resistor is connected in parallel with the coil to reduce the coil's time constant and hence minimize distortion in the early time response.



Figure 6. Photograph of a receive loop antenna.

The use of ferrite material in the core of the receive coils increases the magnetic flux, magnetic field intensity, and in turn the radiation resistance, making the coil receive more efficiently. Relative to air-cored coils, the mutual coupling of ferrite-cored coils is small when they are placed close to each other. Mutual couplings between coils in a receiver array substantially affects the receiver and hence system performance. Minimum couplings are needed to keep receiver array elements sufficiently close for satisfactory performance, and reduction of size and cost of the system. These desired characteristics are not typically achieved simultaneously using conventional EMI receiver array design, which obtains minimum couplings by spatially locating the elements far apart, making the system large and unwieldy.

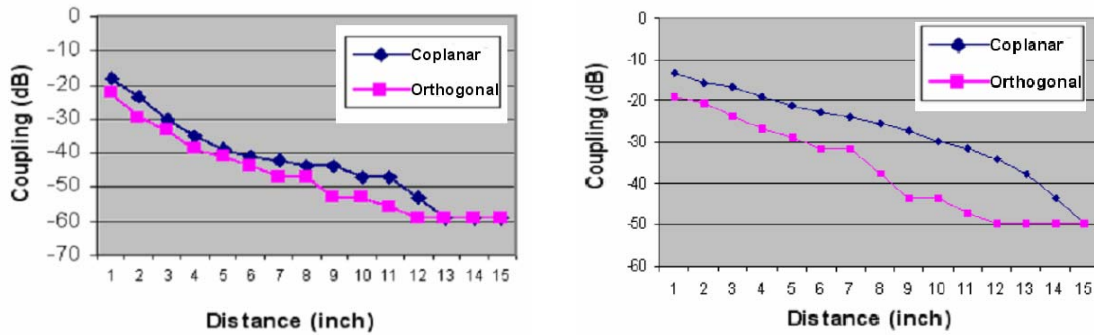


Figure 7. Mutual coupling versus distance between two receiver coils (*a, left*) with ferrite and (*b, right*) without ferrite.

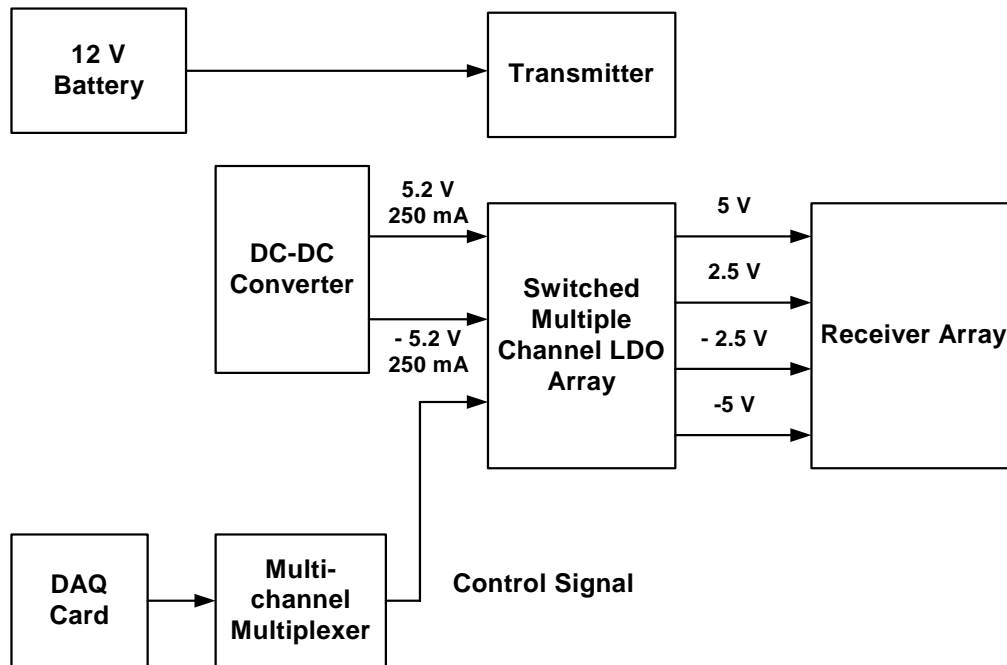


Figure 8. Block diagram of the power supply subsystem shown connecting with the transmitter and receiver.

The calculated magnetic field distributions for receiver coils with and without ferrite indicate that mutual coupling is significantly less for a ferrite-cored coil. Figures 7a-b show experimental results of mutual coupling between two coils with and without ferrite. The ferrite-based coils have much less coupling for both coplanar and orthogonal arrangements, demonstrating the significant coupling reduction when ferrite is used. The measured voltage received by the coil with ferrite is about three times of that received by the coil without ferrite.

1.4 Power Supply Subsystem

A compact, light weight power supply subsystem, providing power for the transmitter and multi-channel receiver, is needed for a man-portable EMI sensor. Our developed power supply subsystem is very compact and integrated directly with the transmitter and receivers on the same circuit board. Figure 8 shows the block diagram of the power subsystem which provides power to the transmitter and receiver array.

The main components of the power supply subsystem are the DC-to-DC converter and low-voltage-drop regulators. The power supply subsystem operates from a 12-V rechargeable portable battery. It converts the 12-V DC input into the stable ± 5 -V and ± 2.5 -V DC voltages with 400-mA current to drive the transmitter and receiver. The multi-channel receiver of the sensor works sequentially, in which only one channel receives responses from targets while others are in stand-by mode. To reduce the power consumption, the DC voltages supplied to the stand-by channels are shut-off. To facilitate this stand-by operation, a controllable switched multi-channel low drop-out (LDO) regulator array has been designed and used in the power module. This LDO array also helps reduce the cross talk between the transmitter and multi-channel receiver, as well as the cross talk between different receiver channels. The LDO array is controlled by the signal from the data acquisition (DAQ) card in the processing unit, which is synchronized with the control signal on the receiver array multiplexer.

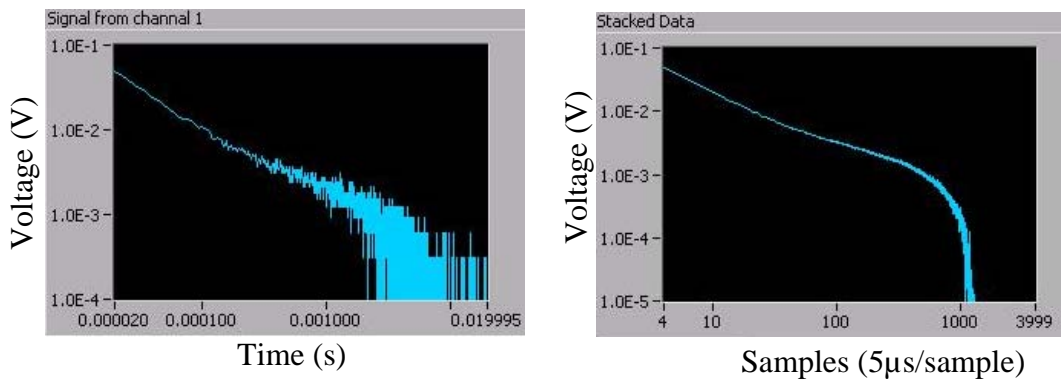


Figure 9. (a, left) Single measurement result. (b, right) Average of multiple measurement results.

1.5 Signal Processing

The signal processing (SP) is realized using the Labview® programming language (National Instruments, Austin, Texas). The SP instructions control the entire system and records the measured data in a laptop computer. The signal processing also stacks, or averages, the results from multiple measurements made for the same target in order to reduce the random component of environmental noise picked up by the receiver coils. A 100-fold stack for each target is recorded by the sensor measurements but only the average, stacked result is recorded into the disk file. Experimental results show that the signal-to-noise-ratio (SNR) is greatly increased by stacking, in accordance with the \sqrt{n} expectation for colorless random noise, where n is stack number. Figure 9 shows results from a single measurement and an average of multiple measurements for the same target.

1.6 Complete System Prototype

Figure 10 shows the block diagram of the developed multi-sensor EMI system. Labview processing code is used along with the DAQ card to control the transmitter and multi-receiver subsystems, acquire data from the DAQ card, and write the data into a disk file in a laptop computer.

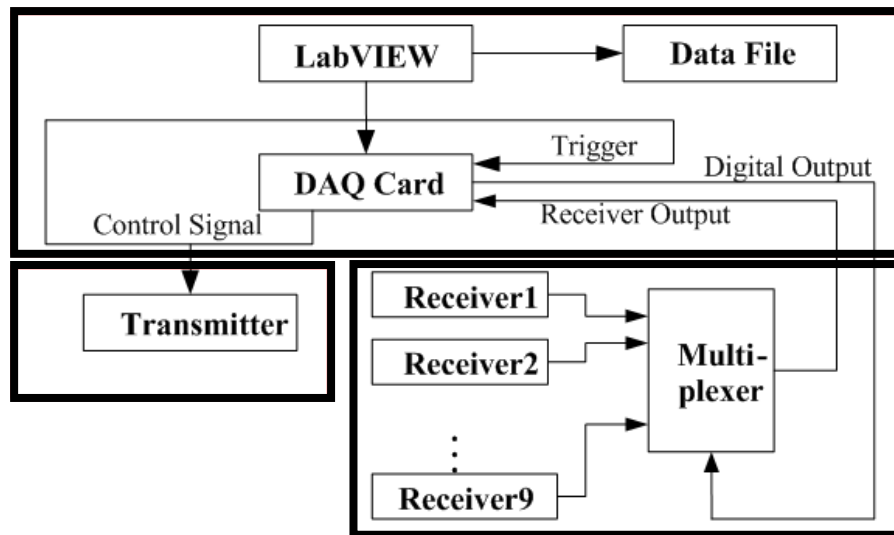


Figure 10. Block diagram of the multi-channel EMI system.

The signal processing flow chart, developed in the Labview environment, is shown in Figure 11. At the start of the operation, the system initiates a measurement with the input of several parameters, such as the transmitter on/off time, data acquisition time and duration. A single receiver coil is then selected by sending a digital signal to the multiplexer.

The total measurement duration, during which a receiver coil is selected to operate, is defined at the beginning of the Labview program depending on the particular

environment. Typically, the measurement duration is set for 100 ms. After a receiver coil is chosen, the EMI response signal from a target that is picked up by the receiver coil is sent to the analog input of the DAQ card, which does not start the data acquisition until it is triggered by a trigger signal. At the same time, the system also turns on the transmitter, producing a current in the transmitter coil. The current flows in the transmitter coil for 40 ms to ensure that all transient responses have vanished. Then the system shuts off the transmitter by sending a control signal. At that time, the data acquisition is triggered by a signal from the DAQ card. The total data acquisition time is 20 ms (later it was set to 40 ms), which can also be adjusted by the Labview program. Figure 12 shows the various duration times for a single data acquisition process.

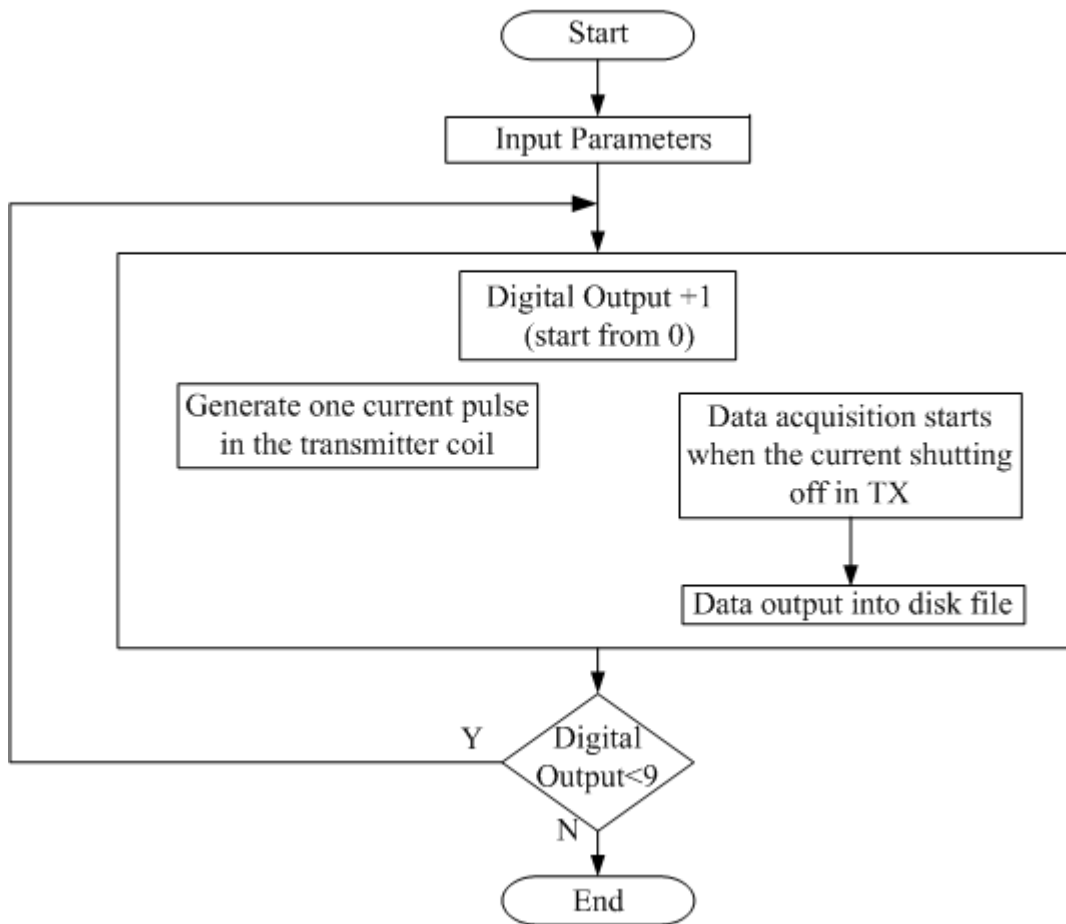


Figure 11. Labview-based program diagram

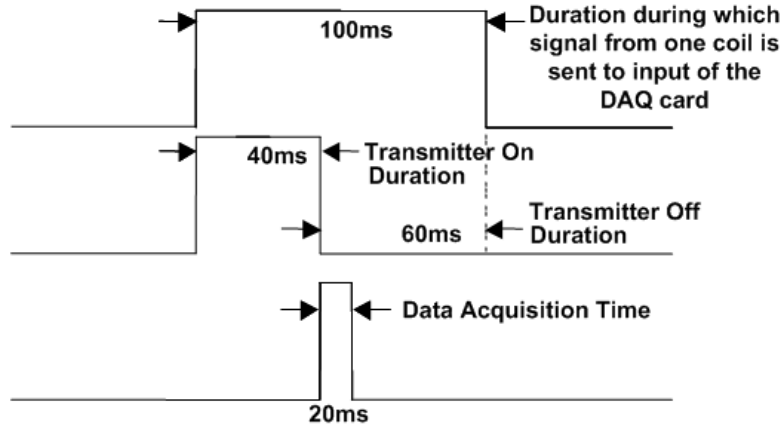


Figure 12. Specified duration time for one data acquisition process.

Figure 13 shows the overall circuit architecture of the EMI UXO prototype system. The layout includes the transmitter, receiver, and power supply module – all integrated into one double-layer printed circuit board. This circuit board is mounted inside a grounded aluminum box to avoid any interference that may distort the system’s performance.

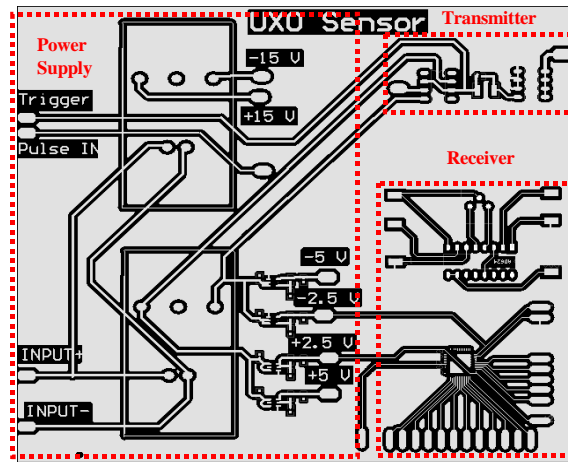


Figure 13. Layout of the EMI sensor printed-circuit board including transmitter, receiver, and power supply subsystem.

Figure 14 shows a photograph of the EMI system board as it is housed in the aluminum box, which during field data acquisition is mounted on the handles of the instrument cart.

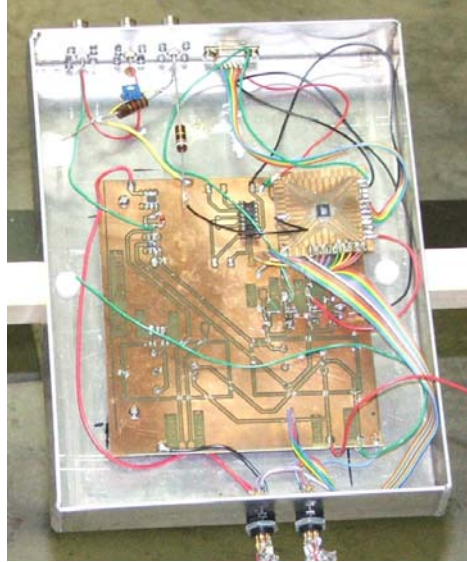


Figure 14. Photograph of the EMI sensor circuit board, consisting of transmitter, receiver and power supply subsystem on a single circuit board, inside an aluminum box. The size of the sensor board is 15.5 cm by 13 cm.

Task 2. Software Development

A long term goal of the EMI UXO research community is to develop new tools for near real-time classification of geophysical responses using time-domain EMI measurements based on multi-transmitter (Tx) multi-receiver (Rx) data acquisition. The UX-1312 software development has provided a significant step toward achieving this goal.

The UX-1312 hardware described in the previous section enables multi-channel acquisition of transient EMI responses from buried UXO targets. It is the objective of the EMI interpretation software to discriminate UXO from non-UXO such as clutter or exploded metal fragments and, furthermore, to classify UXO into various categories such as mortars, artillery shells, submunitions, etc. The UXO/clutter/fragment discrimination and UXO classification rests on an interpretation of the EMI transients in terms of target parameters such as location, depth, orientation, shape, electrical conductivity and magnetic permeability. The EMI interpretation is cast as a parametric nonlinear inverse problem. The discrimination and classification algorithms which follow the inversion process are treated as pattern recognition tasks.

2.1 Nonlinear inversion of EMI transients

Many nonlinear methods for solving inverse problems perform well only near the solution, making selection of the initial model critical to achieving convergence. Continuation or homotopy methods reduce the dependence on the initial model by modifying the original inverse problem. An extra set of nonlinear equations, whose

solution is prescribed, is introduced into the cost function and weighted by an auxiliary parameter λ . The method then relies on tracking paths in the augmented model space from the prescribed solution to the solution of the original problem.

The UX-1312 system has adopted such a numerical continuation approach to solve the non-linear least squares problem for UXO discrimination based on multi-receiver EMI data. The forward model corresponds to a stretched-exponential decay of eddy currents induced in a permeable spheroid. We formulate an over-determined, or under-parameterized, inverse problem. An example using synthetic multi-receiver EMI responses illustrates the advantages of the method. The inversion of actual field multi-receiver EMI responses of inert, buried ordnance is also shown in this report.

A key feature of parametric data interpretation process is model dimension reduction. The most widely-used dimension reduction method is inversion of the data using a low-dimensional forward model that is simple yet can sufficient describe the target response. Under the requirements of UXO cleaning operations, the adopted inversion method must be fast, robust, and almost independent of the subjective bias and training of the instrument operator. The inversion should provide parameters whose values are invariant with respect to the sensor-target configuration but highly dependent on the geometry and physical properties of the target.

2.1.1. The inverse problem

Inversion of geophysical data consists of finding a model vector \mathbf{b} that reproduces the most important features of a set of observations \mathbf{d} using a physically justifiable forward model $f(\mathbf{b})$. The forward model in most cases is nonlinear. The “best” model \mathbf{b}^* minimizes a scalar cost, or objective, function that measures the goodness of fit between the observations and the forward model response. The most widely used cost function is based on the L_2 least-squares norm. The non-linear inverse problem is traditionally solved by Newton-Raphson, Gauss-Newton, Levenberg-Marquard, Powell’s methods (Madsen et al., 2004), or conjugate gradients (Nocedal and Wright, 1999) to cite just a few. It is well-known that geophysical inverse problems are ill-posed and the methods to solve them oftentimes are unstable (Vasco, 1998) due to intrinsic non-uniqueness, over-parameterization, and/or large residuals. The latter is relevant for data with a large dynamic range, such as time-domain EMI responses. If the initial model vector \mathbf{b}_0 is far from the convergence region of a local or global minimum of the cost function, then oftentimes no solution with a tolerable misfit can be found.

2.1.2. Continuation methods

Continuation/homotopy algorithms have long been used for solving nonlinear systems of algebraic equations. These methods, which are convergent for almost all choices of starting point, are broadly applicable to fixed-point problems and zero finding problems (Watson, 1989; Rheinboldt, 1980). In geophysics, continuation methods have been applied using a parameterization based on the arc-length along the continuation path for the inversion of seismic ray-tracing data (Keller and Perozzi, 1983), seismic travel-time

tomography (Vasco, 1994), and multi-frequency EMI data (Jegen et al., 2001). The solution of the regularized inverse problem for seismic cross-well tomography (Bube and Langan, 1999), and the inversion of seismic first arrivals for near-surface velocity structure (Vasco, 1998) showed the advantages of this method to evaluate the misfit vs. model roughness trade-off. An early use of the homotopy method based on formulating the EMI inverse problem as an equivalent set of polynomial equations is provided by Everett (1996).

2.1.3. Forward Modeling

A continuation method for inverting time-domain multi-receiver EMI data has been developed within the context of the UX-1312 project. The aim is to produce a low-dimensional description of a UXO response using a simple physics-based forward model based on a stretched-exponential decaying dipole. The use of a fast, simple dipole forward model (Pasion and Oldenburg, 2001; Zhang et al., 2003) satisfies both the near real-time UXO decision requirement, and the necessity of using model parameters with target discrimination capabilities. Near real-time processing rules out more accurate but time-consuming approaches such as a full Maxwell differential-equation-based solution of the EMI forward problem for complicated geometries and high conductivity and permeability contrasts using finite difference or finite element methods. The use of closed-form solutions for the EMI response of simple geometrical shapes such as a hollow sphere (Mrozynsky, G., 1998) or a prolate spheroid (Ao et al., 2002) in free space was considered as an alternate forward modeling paradigm but these solutions are not able to cope with a wide range of target responses for different sensor-target geometries.

2.2. Inversion: algorithmic details

Define a vector $\mathbf{d} = (d_1, d_2, \dots, d_n)^T$ representing the spatiotemporal EMI response from a buried target. Each datum is associated with a vector \mathbf{x} of independent variables, consisting of Rx coil location and orientation, transmitter (Tx) location, Tx current, and a list of the time gates at which the EMI response is sampled. The physics-based forward model capable of predicting the data vector is defined as $f(\mathbf{x}, \mathbf{b})$, where $\mathbf{b} = (b_1, b_2, \dots, b_p)^T$ is the vector of model parameters. An auxiliary continuation or homotopy parameter is introduced, and denoted as λ . For the inversion process, the $(p+1)$ -dimensional search space is the one that is spanned by the augmented model vector (\mathbf{b}, λ) . The augmented cost function to be minimized is

$$(1) \quad S^\lambda(\mathbf{b}) = \frac{1}{2} \|\mathbf{F}^\lambda(\mathbf{b})\|_2^2 + \sum_{j=1}^p G(\mathbf{b}_j).$$

Equation (1) consists of an augmented L_2 -norm misfit and a set of penalty terms G operating on the model vector \mathbf{b} . The standard and augmented residuals are defined as

$$(2) \quad F_i(\mathbf{b}) = f(\mathbf{x}_i, \mathbf{b}) - d_i,$$

$$(3) \quad \mathbf{F}^\lambda(\mathbf{b}, \lambda) = \mathbf{F}(\mathbf{b}) + (\lambda - 1)\mathbf{F}(\mathbf{b}_0).$$

The augmented residual (equation 3) combines the standard residual vector $\mathbf{F}(\mathbf{b})$ and a constant vector $\mathbf{F}(\mathbf{b}_0)$ describing the residual of the starting model \mathbf{b}_0 . Define \mathbf{b}^* as the standard least-squares solution to $\mathbf{F}(\mathbf{b})=0$. The continuation method minimizes a discrete sequence of augmented cost function $S^\lambda(\mathbf{b})$ starting with the cost function $S^0(\mathbf{b})$ that is associated with $\lambda=0$ and terminating with the cost function $S^1(\mathbf{b})$ associated with $\lambda=1$. The discrete sequence is generated by varying the parameter λ in steps of $\Delta\lambda$ from the starting value $\lambda=0$ to the ending value $\lambda=1$. For each value of λ , an optimal model \mathbf{b}^λ is determined by minimizing $S^\lambda(\mathbf{b})$. The continuation method in this way generates a discrete sequence \mathbf{b}^λ of optimal models in $(p+1)$ -dimensional space from the *a priori* selected starting model $\mathbf{b}^0 = \mathbf{b}_0$ to the final model $\mathbf{b}^1 = \mathbf{b}^*$. The latter shall represent the solution to the nonlinear inverse problem. In the continuation method, the path tracked in the augmented model space from $\lambda=0$ to $\lambda=1$ must be one that maintains the cost function near zero, $S^\lambda(\mathbf{b}) \sim 0$.

The use of the penalty terms in the cost function is to keep the model parameters within well-defined bounds. Out-of-bounds model parameters are penalized by a high cost. We have chosen the following sigmoidal penalty function $G(\mathbf{b}_j)$, characterized by a nearly constant cost inside the allowed region and steep walls rising to a very high cost at the boundaries,

$$(4a) \quad G(\mathbf{b}_j) = A [2 + \tanh(\theta b_{2j}) - \tanh(\theta b_{1j})]$$

$$(4b) \quad b_{2j} = (b_j - b_j^{\text{MAX}}) / (b_j^{\text{MAX}} - b_j^{\text{MIN}})$$

$$(4b) \quad b_{1j} = (b_j - b_j^{\text{MIN}}) / (b_j^{\text{MAX}} - b_j^{\text{MIN}})$$

In these equations, the adjustable parameter θ controls the steepness of the boundary wall and $b_j^{\text{MAX}}, b_j^{\text{MIN}}$ are the pre-determined upper, lower limits for the model parameter b_j . A suitable amplitude A is determined after the standard misfit is calculated following the first iteration.

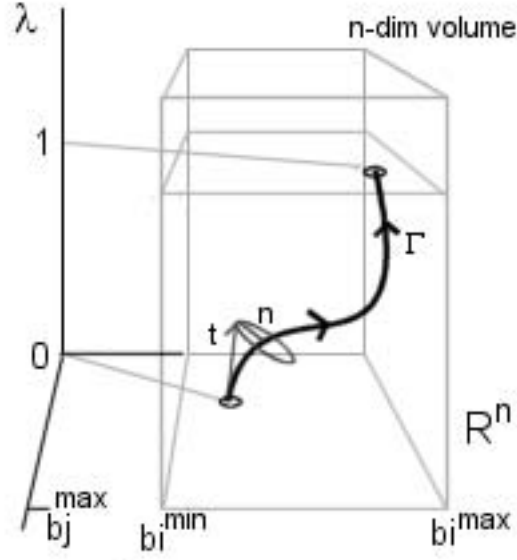


Figure 15. Schematic of a continuation path Γ in a bounded search hypercube. The path starts at $\lambda = 0$, following a series of predictor step (t) and a corrector step (n) that should be inside the convergence radius of the corrector in order to find the new continuation point.

The path-tracking through the augmented model space can be accomplished in several ways, each providing the discrete equivalent of a smooth, continuous, non-bifurcating, non-divergent path along which $S^\lambda(\mathbf{b}) \sim 0$ (Garcia and Zangwill, 1981; Watson, 1989). The predictor-corrector approach we use in this work is based on predicting the next point along the path and then correcting its position using a Gauss-Newton (GN) sequence of iterations (see Figure 15). At the k -th homotopy parameter step, with $\lambda = \lambda_k$, the GN correction updates the model vector using the equation (De Villiers and Glasser, 1981)

$$(5) \quad \mathbf{b}_{k+1} = \mathbf{b}_k - \mu [\mathbf{div}^2 S^\lambda(\mathbf{b}_k)]^{-1} \mathbf{div} S^\lambda(\mathbf{b}_k).$$

The second term on the right-hand side contains the negative gradient, and the Hessian matrix (inside the square brackets) scaled by stepsize μ . The gradient is calculated analytically while the Hessian is calculated using the approximation for small residuals (Nocedal and Wright, 1999) or forward differences. A singular value decomposition (SVD) algorithm is used to calculate the pseudo-inverse of the Hessian matrix. The predictor step should be small enough to allow the GN corrector to converge in a few iterations. Three corrector-step stopping criteria are used based, respectively, on variation of the updated model vector, variation of the cost function value, and the value of the gradient. Once the corrector step is terminated, the next predictor step is initiated. Following the zero path $S^\lambda(\mathbf{b}) \sim 0$ by this series of predictor and corrector steps from its start point $\lambda = 0$ to its endpoint $\lambda = 1$ at high accuracy generally is not difficult until the endpoint $\lambda = 1$ is approached. At the endpoint, the predictor step-length and corrector stop conditions must be modified in order to maintain the accuracy of the path tracking.

2.2.1. Stretched exponential

The physics-based EMI forward model corresponds to a transient, decaying magnetic dipole source $\mathbf{m}(t)$ located at \mathbf{r}' that induces a voltage in a receive coil located at \mathbf{r} with normal vector \mathbf{n}^{RX} of the coil axis. The spatiotemporal EMI response is

$$(6) \quad f(\mathbf{r}, \mathbf{r}', \mathbf{b}, t) = -d/dt \mathbf{T} \mathbf{m}(t) \cdot \mathbf{n}^{\text{RX}}$$

where \mathbf{T} is the dyadic $\mathbf{T} = \text{div} \text{div}(1/r)$. In order to model the response of axi-symmetric targets, we use an empirical “stretched-exponential” model which describes the superposition of two magnetic moment vectors, one directed along the principal axis of the spheroid $\hat{\mathbf{a}}$ (subscript L), and the other pointing in the direction of the primary field \mathbf{B}^{TX} (subscript T),

$$(7a) \quad \mathbf{m}(t) = (\gamma_L - \gamma_T) (\mathbf{B}^{\text{TX}} \cdot \hat{\mathbf{a}}) \hat{\mathbf{a}} T_L(t) + \gamma_T \mathbf{B}^{\text{TX}} T_T(t).$$

The polarizability parallel and transverse to the principal axis are denoted by γ_L and γ_T , respectively. Notice that each term on the right hand side of equation (7a) decays at a different rate, $T_L(t)$ or $T_T(t)$, where

$$(7b) \quad T_L(t) = d/dt \{ t^{-\beta_L} \exp [(-s_L t)^{1-\beta_L}] \},$$

$$(7c) \quad T_T(t) = d/dt \{ t^{-\beta_T} \exp [(-s_T t)^{1-\beta_T}] \}.$$

In these equations, $\beta_{L,T}$ and $s_{L,T}$ are the stretching coefficients and decay rates, respectively. Among several possible candidates for $T(t)$, we choose the stretched exponential induced current decay because it provides a simple and effective temporal description of the EMI data that agrees with our field experience. The stretched exponential form is physically justifiable since it describes an eddy current generation mechanism in a heterogeneous target that is based on a multiplicative process (Laherrère and Sornette, 1998). Similar multiplicative processes have been reported for remanent magnetization decay in spin-glasses (Chamberlin et al, 1984) and dielectric relaxation (Williams and Watts, 1970). Stretched exponential decays are broad-band, continuous functions that can be interpreted in terms of an assemblage of interacting eddy current modes co-existing in a geometrically complex target.

2.2.2. Data acquisition

Parallel to the design and development of the UX-1312 multi-receive prototype, controlled source EMI data were acquired using a modified Geonics EM63 time-domain metal detector (Geonics, 2002). The commercial EM63 system uses a Tx bipolar square waveform with base frequency of 5 Hz, delivering a maximum current intensity of 16 A. Transients are recorded at 26 geometrically time-spaced gates from 177 μs to 25 ms. The EM63 is a cart-mounted central-loop configuration system. When it is used in wide-area surveying mode, a single transient is recorded at each Tx location.

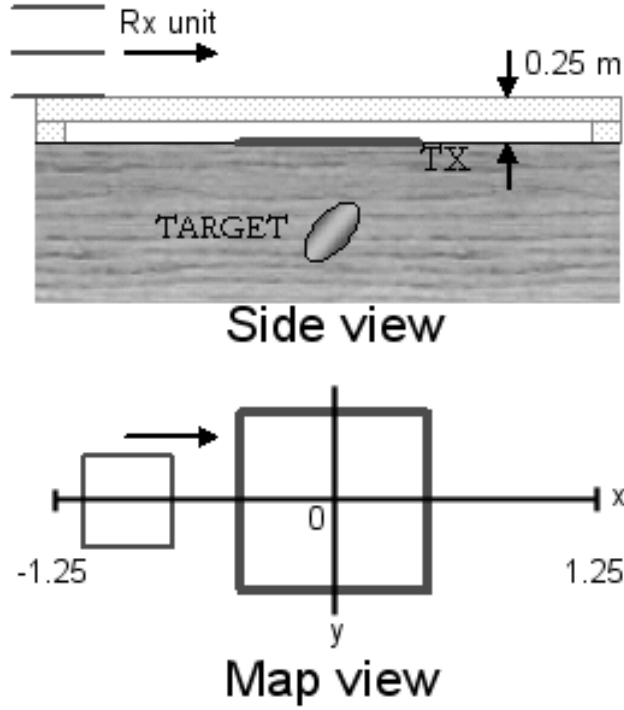


Figure 16. Schematic of the experimental setup using a modified Geonics EM63. The Rx unit is moved along the wooden structure. The detected target is positioned about the center of the Tx coil.

We modified the system geometry by separating the Rx and Tx coils (Everett *et al.*, 2005). A custom-adapted 4.0 m cable supplied by Geonics and a simple 3.0 m long wooden structure allows multi-Rx location data acquisition while the Tx coil remains fixed, in this case, laid on the ground surface (Figure 16). The Rx unit is moved along the wooden structure, sampling the temporal EMI response each 0.1 m along a 2.5 m profile in the x -direction. Combining the temporal response at each station generates the full EMI spatiotemporal response of the target and background. Each spatiotemporal response corresponds to 25 Rx locations and comprises $\sim 1,500$ transients.

Spatiotemporal responses were acquired by burying a target at some depth (between 0.4 m and 0.5 m) centered on the Tx coil. The central burial is not necessary for our method to work but is chosen here since it achieves maximum Tx-target electromagnetic coupling. Background responses were also measured before and after each acquisition protocol to enable an estimate of the background-subtracted free-space target response and to monitor Tx current stability. Raw target responses were stacked at each Rx location to produce enhanced signal-to-noise ratio (SNR). For the present paper, we assume that the mutual electromagnetic coupling between the target and the background geological medium is negligible so that the total EMI response is a simple, linear superposition of both target and background responses. The background-subtracted (BGS) data (Figure 17) is then used during the inversion process. During actual UXO prospecting, the background response without the target present cannot be known. In that case, we recommend that BGS data are formed using spatial averaging of background EMI

readings taken in the vicinity of a putative UXO target. Initial values for the model parameters $\hat{\mathbf{a}}$ and \mathbf{r}_o were kept fixed for different model vectors chosen. The experimental setup constrains the horizontal location of the target while the vertical coordinate can be made by cursory inspection of the maximum, asymmetry, and width of the spatial EMI response.

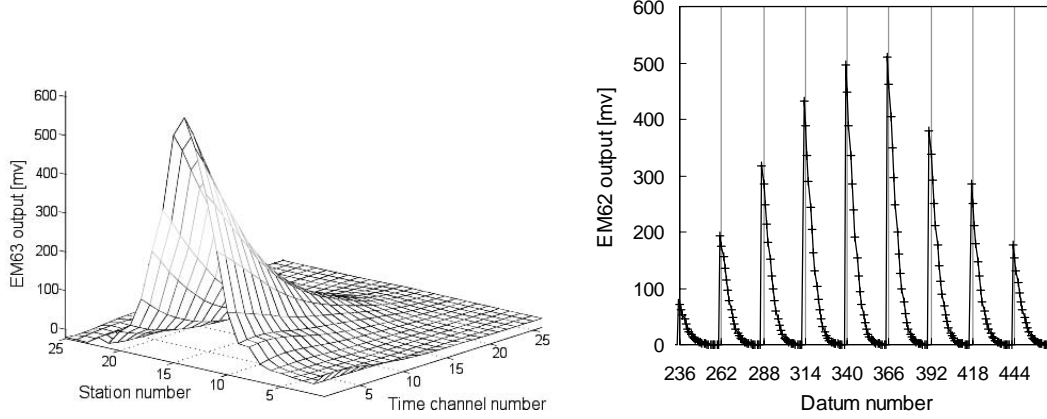


Figure 17. (a, left) 50mm M22 ordnance spatiotemporal response as a 3-D surface. At Each station, an averaged transient is recorded (lines parallel to the time channel number axis. Each node in the surface corresponds to a Rx output voltage, or datum. (b, right) The spatiotemporal response is represented as a 1-D vector of appended transients starting from station 1. Each transient contains 26 log-spaced data points.

2.3. Results and discussion

Two inversion examples are discussed here to illustrate the performance of the continuation algorithm. The 12-dimensional model vector in both cases corresponds to the forward model described by equations (7a-c), and it is ordered as follows $\mathbf{b}=(\gamma_L, \gamma_T, \hat{\mathbf{a}}, \mathbf{r}_o, \beta_L, \beta_T, s_L, s_T)$. The decay rates s_i are expressed in ms. The initial model \mathbf{b}_0 is the same in both examples.

2.3.1 Synthetic data

A synthetic data vector was generated using the following model vector $\mathbf{b}=(1.14, 0.08, 0.8551, 0.0, 0.5184, 0.12, 0.1, 0.25, 0.1, 0.3, 0.5, 3.5)$, corresponding to the target principal axis $\hat{\mathbf{a}}$ inclined 31.23 degrees in the x-z plane. The target is located at 0.25 m below the $z = 0$ plane, and the longest eddy current decay is along the $\hat{\mathbf{a}}$ direction. The synthetic data were contaminated by Gaussian noise to produce a $\text{SNR} = 20$. The synthetic Tx coil consisted of a 1.0 x 1.0 square coil driven by 1 A electric current placed 0.025 m above the ground surface to simulate our modified EM63 multi-Rx data.

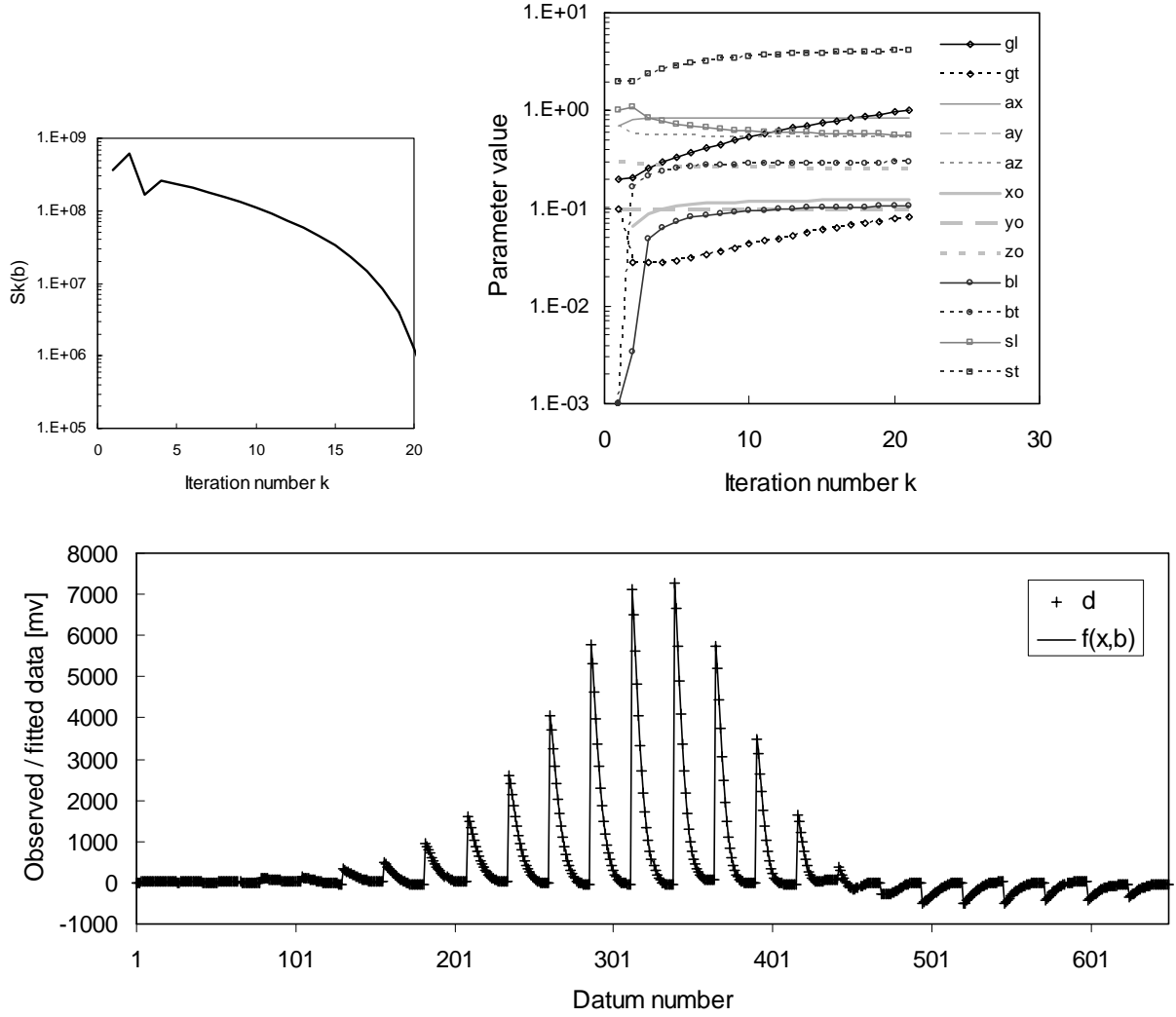


Figure 18. Inversion results for a synthetic dataset corresponding to a stretched-exponential decaying magnetic spheroid. The data is contaminated with Gaussian noise having a SNR = 25. (a) The resulting cost function value as a function of the predictor iteration number. (b) Model vector evolution during the path tracking. At iteration 20, the continuation parameter $\lambda = 1.0$, providing the solution to the initial non-linear problem. (c) Data vector and final model solution.

The continuation algorithm was initiated using this starting model. The path step length was selected as $\Delta\lambda = 0.05$. For the corrector step, stopping tolerances were set to 10^{-3} for the cost function and model vector variations, respectively. The maximum number of corrector iterations, at each predictor step, was set to 5 and a SVD threshold of 10^{-5} was established for the Hessian pseudo-inverse computation. The initial model vector was chosen to be $\mathbf{b}_0 = (0.1, 0.1, 0.7071, 0.0, 0.7071, 0.0, 0.0, 0.3, 0.001, 0.001, 1.0, 2.0)$. Figure 18a shows exponential convergence of the inversion with the predictor iteration number, reducing the cost function value by almost three orders of magnitude.

The path tracking in the augmented model space is visualized in Figure 18b. Smooth evolution of each model parameter is observed after the third predictor step. Variations of more than two orders of magnitude in transversal stretched coefficient β_T and decay rate s_T reflects the attempts of the algorithm to fit the model vector to the small amplitude decay in the direction of the primary field. The model vector found for $\lambda = 1.0$ was $\mathbf{b}_* = (1.04, 0.08, 0.837, -9.68 \times 10^{-12}, 0.5464, 0.12, 0.15, 0.26, 0.11, 0.29, 0.56, 4.1)$. The CPU time using a Pentium IV processor was $t = 5.5$ s and the distance between the starting and final models is $\|\mathbf{b}_* - \mathbf{b}_0\| = 2.35$. For comparison, the inversion of perfect data (0% Gaussian noise added) matched the true model in $t = 4.9$ s with $\|\mathbf{b}_* - \mathbf{b}_0\| = 1.01$. The excellent fit between the synthetic data and the EMI spatiotemporal response of model \mathbf{b}_* is shown in Figure 18c. An equivalent attempt to perform the inversion using a standard Gauss-Newton algorithm failed to converge. The SNR chosen for this example resembles the one we find in time-domain EMI experiments using the modified EM63. The inversion result described here constitutes a reasonable gauge of the capability of the continuation algorithm to recover physically interpretable values for the stretched coefficient and decay rates.

2.3.2 EMI field data

An inversion of actual field-measured EMI spatiotemporal data corresponding to a buried 57mm M22 ordnance is shown next. The 57mm M22 is a small-size artillery round ordnance 17.1 cm long and 5.7 cm in diameter. The EM63 multi-Rx data were acquired with the ordnance buried at 0.2 m (depth below surface to the top of the ordnance). The axis of symmetry was inclined about 45 degrees with respect to the vertical with the nose pointing down in the positive x-direction.

The initial model vector was kept the same as in the synthetic inversion, but we found it necessary to change to 10 the maximum number of iterations for the corrector step and to 0.4 the step size of the Gauss-Newton correction. We also used a longer predictor step size, $\Delta\lambda = 0.1$. This time, the depth-to-target parameter is made adjustable. The continuation inversion was performed in 6 s of CPU time with a “total path length” of $\|\mathbf{b}_* - \mathbf{b}_0\| = 1.85$. The final model at $\lambda = 1.0$ was $\mathbf{b}_* = (0.2506, 0.0012, 0.9796, 0.0, -0.2007, 0.1296, 0.0, 0.2928, 0.0137, 0.2458, 0.0732, 0.7946)$. There is a much stronger longitudinal eddy current response that lasts longer than the decay directed along the primary field. The inverted depth value matches the burial depth to the central portion of the ordnance.

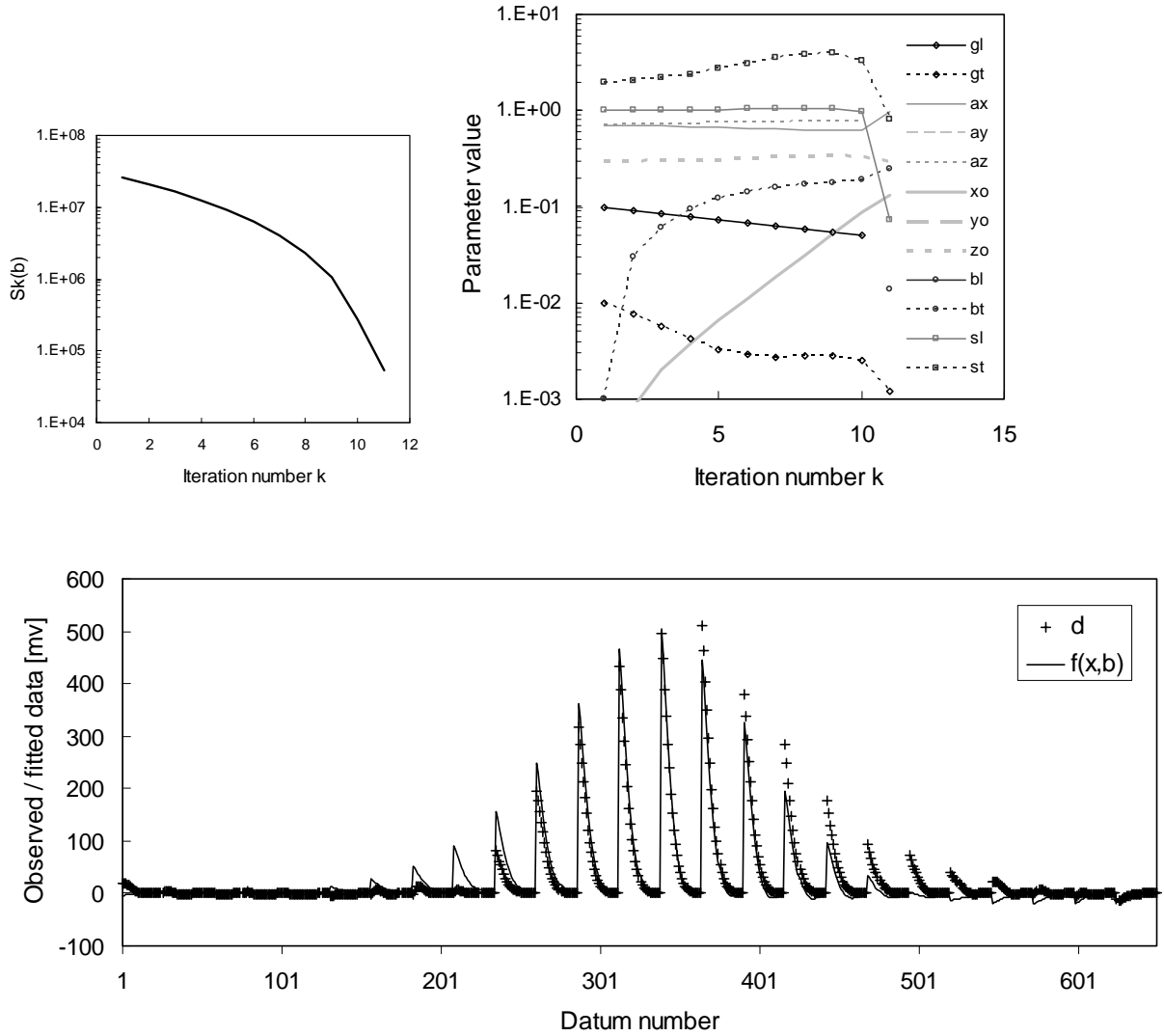


Figure 19. Inversion results for a 57mm M22 ordnance, buried at 0.2 m (depth to the topmost part) at 45 degrees with respect to the horizontal with the nose pointing down towards the positive profile direction. (a, *top left*) The resulting cost function value as a function of the predictor iteration number. (b, *top right*) Model vector evolution during the path tracking. Notice the exponential convergence at the final continuation steps. (c, *bottom*) Data vector and the final model solution.

The cost function (Figure 19a) shows again a very fast convergence within only 10 prediction steps. The parameter evolution (Figure 19b) shows considerable topological complexity in the tracked $(p+1)$ -dimensional path compared to the relatively simple path obtained for the synthetic inversion. Note that the polarizabilities and decay rates become less sensitive to changes in the continuation parameter λ during the last 3-4 predictor steps. This means that near the endpoint $\lambda=1$, there is a wider range of values that can be chosen to fit the data without affecting the cost function considerably. In other words, variations in those parameters, or combinations of them, produce similar EMI responses,

i.e. there is a degeneracy in the model parameterization. A certain amount of model equivalence, as a degenerate parameterization is otherwise known, is an inevitable characteristic of any nonlinear geophysical inversion. Again, an attempt to perform the inversion using a standard Gauss-Newton algorithm failed to converge using the same settings.

2.4. Inversion: conclusions

A continuation method for non-linear inversion of transient multi-receiver (spatiotemporal) UXO responses apparently reduces the necessity of choosing an initial model close to the one that minimizes the cost function. We have shown with two representative examples that continuation path tracking through a low-dimensional model space is stable enough to reliably invert spatiotemporal EMI data. Mapping the evolution of model parameters along the path is a useful tool to assess the robustness of the final model and to detect degenerate parameterization or unimportant parameters. There is a wide range of possibilities to improve the convergence of the current algorithm. These include damping the Hessian matrix inversion or parameterizing the continuation path as a function of arc-length.

The CPU time required for performing the inversion is in the range of seconds, so it is possible to implement this algorithm in near-real time directly on the field data acquisition platform.

2.5 Feature extraction and classification of EMI responses

The overall objective of the software task for the UX-1312 project is to develop UXO discrimination capabilities based on multi-receiver time-domain EMI data. The key steps are experimental design, data acquisition, physics-based nonlinear model inversion, the creation of a target response feature library, and a feature-based classifier. In this section of the report we shall describe the initial testing of a feature-based classifier using modified EM63 data.

As described above, the requirements of near-real time discrimination routines suggest the use of computationally inexpensive forward models for describing target responses. It is thought that simple physics-based or empirical models are able to account for variations in target responses between different target categories or burial configurations. The resulting model parameters, estimated from the target EMI responses via nonlinear inversion, constitute the input data for extracting those parameters or *features* that can be useful for classification purposes. Useful features for the classifier software are those model parameters that provide information on target geometry but are relatively insensitive to details of the relative orientation and position of the sensor with respect to the target. The term *feature vector* refers to the subset of model parameters that has UXO discrimination capabilities.

Spatiotemporal EMI data were acquired using the modified EM63 multi-RX setup shown in Figure 16. Targets from the U.S. Army inert UXO kit were buried in the various

configurations shown in Figure 20, which also shows that TX loop orientation and the data acquisition profile. Recall that the TX loop is held in a fixed position while the RX loop is moved along the acquisition profile.

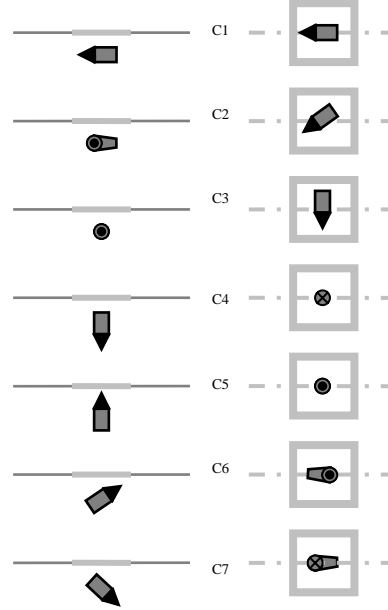


Figure 20. The various burial configurations of inert UXO items used for feature extraction and classification of EMI responses. (*left*) vertical section, showing Earth surface and side view of EM63 TX loop. (*right*) plan view, showing data acquisition profile (dotted line) and top view of EM63 TX loop.

The physics-based EMI forward model used for feature extraction is the empirical stretched-exponential formula

$$(8) \quad \tilde{f}(\mathbf{r}, \mathbf{r}', \mathbf{b}, t) = -\frac{d}{dt} \mathbf{div} \mathbf{div}(1/r) \mathbf{m}(t) \cdot \mathbf{n}^{RX}$$

where \mathbf{T} is the dyadic $\mathbf{T} = \mathbf{div} \mathbf{div}(1/r)$ and

$$(9) \quad \mathbf{m}(t) = V_0 t^{-\beta} \exp [(-\lambda t)^{1-\beta}] \underline{\mathbf{m}}.$$

In the previous equation, $\mathbf{m} = V_0 \underline{\mathbf{m}}$ is the dipole moment of strength V_0 oriented in the $\underline{\mathbf{m}}$ direction, β is the stretched coefficient and λ is the decay rate. Optimal values of the parameters (V_0 , β , λ) are determined, for each UXO burial configuration, by inverting an EM63-multiRX spatiotemporal response using the nonlinear continuation algorithm described above.

Inversion of EM63-multiRX spatiotemporal responses for optimal (V_0 , β , λ) parameters is indicated in Figure 21. The data were acquired at the Texas A&M Riverside campus UXO test site. The inversion results are displayed as parameter cross-plots of λ -vs- V_0 (*left*) and β -vs- V_0 (*right*). The target is the 40 mm MKII ordnance from the U.S. Army inert UXO kit. The optimal parameters found by nonlinear inversion are plotted using different

symbols for the various burial configurations C1-C7. Multiple symbols of the same type indicate that the UXO was buried in the same configuration at different depths.

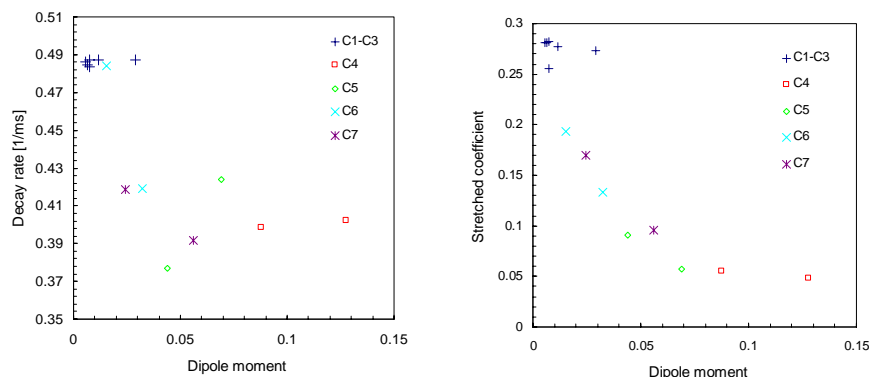


Figure 21. Inversion of EM63-multiRX responses for 40 mm MKII ordnance in the various burial configurations C1-C7.

There is a definite clustering of the parameters according to burial configuration. For example, the C4 burial (vertical UXO placement, nose-down) yields a larger apparent dipole moment V_0 and a smaller stretched coefficient β than the other burial configurations. The apparent decay rate λ is also small when the UXO is buried in the C4 configuration. At the other extreme, burial configurations C1-C3 (horizontal UXO placement) consistently yield, regardless of the strike angle of the UXO with respect to the data acquisition profile direction, a large apparent decay rate λ , a large apparent stretched coefficient β and a small apparent dipole moment V_0 .

A glance at both panels of Figure 21 reveals inverse relationships between the cross-plotted parameters suggestive of a general trade-off between both λ and β with respect to V_0 as the burial configuration is varied. This trade-off could become an important factor as it introduces a measure of ambiguity in UXO discrimination based on spatiotemporal EMI responses.

The clustering of optimal (V_0 , β , λ) parameters for a variety of non-UXO items (a small steel sphere, aluminum plate and copper loop) and items from the U.S. Army inert UXO kit has been examined. Parameter cross-plots V_0 -vs- λ (*top*), V_0 -vs- β (*bottom left*) and λ -vs- β (*bottom right*) are shown in Figure 22. This is an example of 3-D feature space. Multiple symbols of the same type in the parameter cross-plots indicate different burial configurations. Generally, the different targets organize themselves into clusters within parameter space, roughly independent of burial configuration. In other words, like symbols tend to plot close together while unlike symbols plot farther apart. There are several obvious exceptions to this rule.

The loop target is a 15 cm radius 12 gauge circular copper wire whose inverted parameters are shown by the solid blue diamond symbol in the cross-plots. Note that the copper loop generates the same apparent dipole moment V_0 as several of the other targets, including the 40 mm MKII and XM230 ordnance types, as well as a moderate apparent

stretched coefficient, β . However, the loop generates a much larger apparent decay rate λ than any other item. On this basis, for example, we can use the spatiotemporal EMI response to discriminate a loop of copper wire from a buried UXO.

The aluminum plate target denoted 1VP, buried in a vertical orientation (shown as the red cross symbols in the cross-plots), is characterized by large V_0 but small (λ , β) values. The BDU28 submunition (blue star symbols) displays this pattern in certain of its burial configurations. In other burial configurations, the BDU28 generates a small V_0 and a large β . This finding underscores a difficulty of UXO discrimination using EMI spatiotemporal data. The aluminum plate may be confused for the BDU28 submunition, but only in certain burial configurations. In other burial configurations, the two target responses can become well-separated from each other in 3-D feature space.

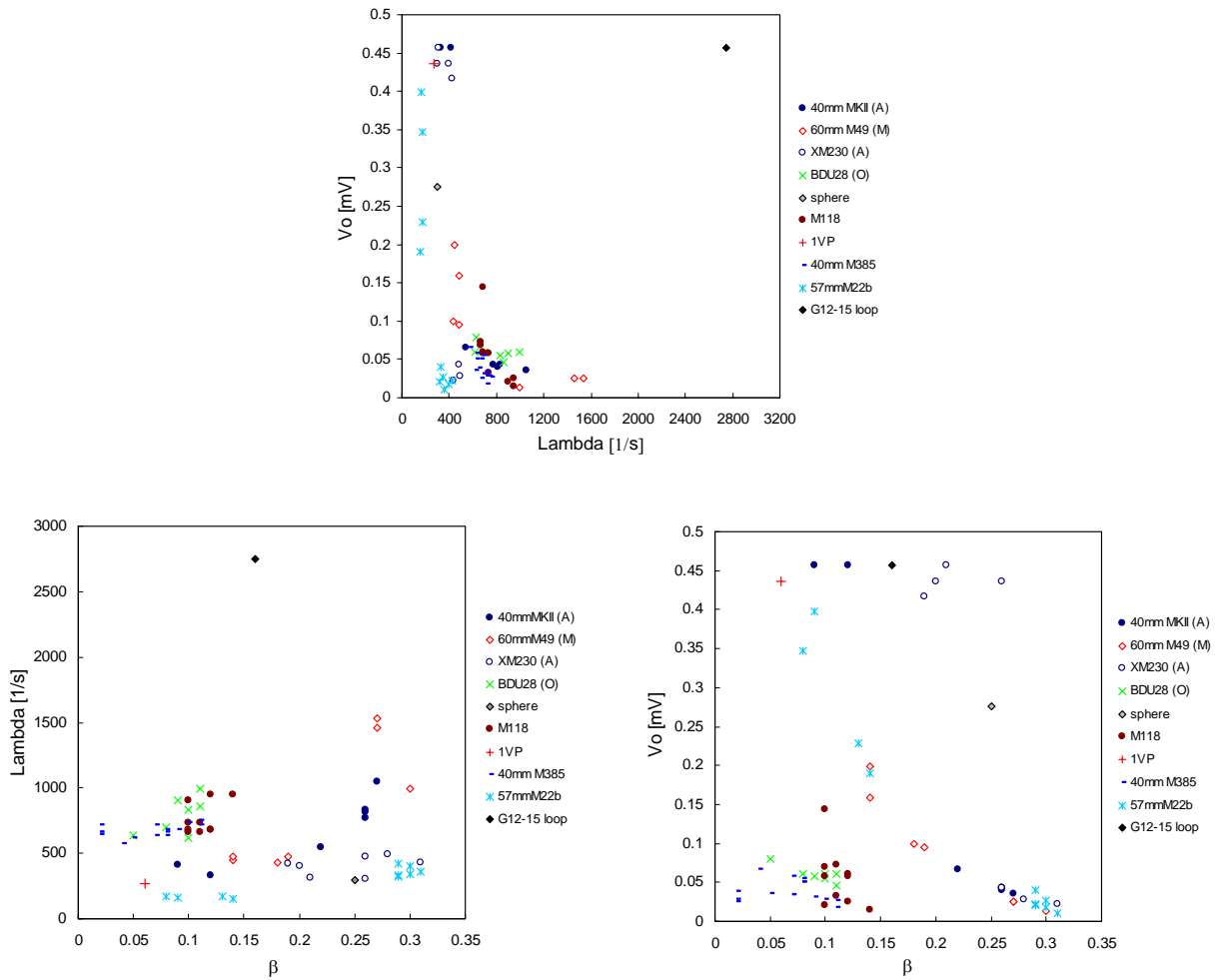


Figure 22. 3-D feature space for a set of UXO and non-UXO targets under different burial configurations and depths.

Cross-plots of the optimal (V_0 , β , λ) parameters for various targets oriented in burial configuration C-1 at 0.2 m depth is shown in Figure 23. In this example, the parameters

from artillery (A), mortar (M) and sub-munitions (O) targets are class-averaged and plotted along with some other targets including non-UXO clutter items such as the steel sphere, copper wire loop and vertical aluminum plate.

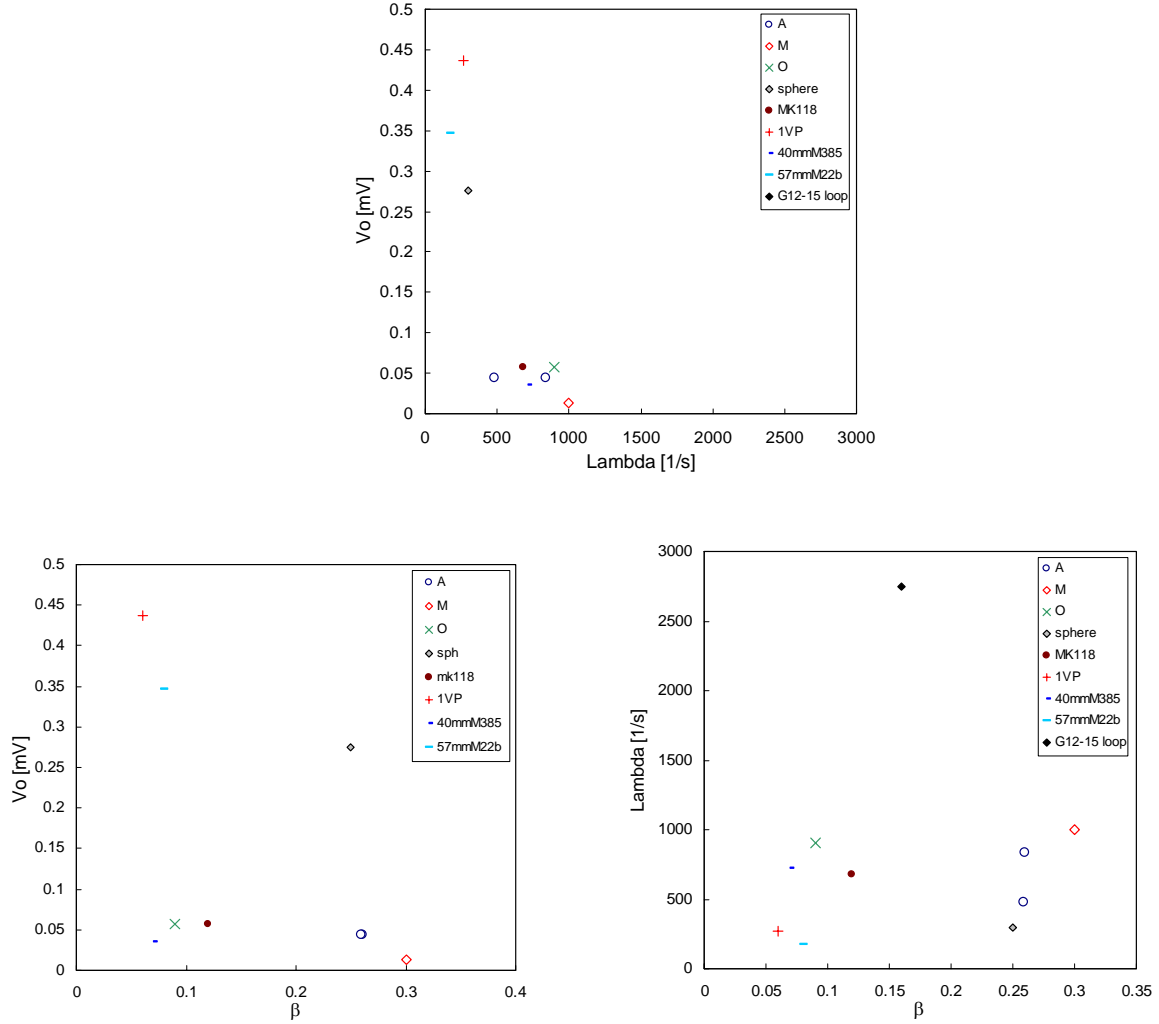


Figure 23. 3-D feature space for a set of UXO and non-UXO targets under burial configuration C-1 and depth 0.2 m. Some of the UXO target inverted parameters are averaged within artillery (A), mortar (M) and ‘submunition (O) classes.

According to Figure 23, the (A,M,O) class-averaged parameters exhibit distinct clustering relationships. For example, the A and M (artillery and mortar) parameters appear in close association with each other in all three cross-plots. No other type of item is consistently close to the (A,M) pairing. The S (submunitions) β parameter is much lower than the corresponding A and M β parameter. This implies that the EMI response of submunitions is distinguished from those of artillery or mortar on the basis of a smaller apparent stretched coefficient. The cross-plots suggest a manner by which UXO/non-

UXO *discrimination* and *classification* of UXO into type may be accomplished using spatiotemporal EMI responses.

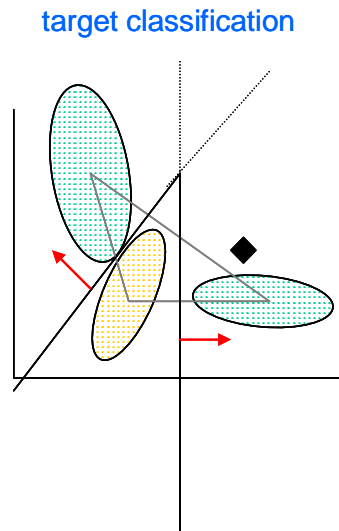


Figure 24. UXO target classification based on linear decision boundaries in feature space.

The accomplishments made during the UX-1312 project in nonlinear inversion and feature extraction based on spatiotemporal EMI responses suggests the feasibility of a feature-based classification scheme shown schematically in Figure 24. In this approach, training data are used to identify regions in feature space within which the parameters associated with a single UXO class clusters. For example, in Figure 24 the three shaded regions may correspond to artillery, mortar and submunitions (A,M,O) classes. Alternatively, parameters from a single UXO class may cluster into a multiply connected region of feature space according to burial configuration.

The various regions of feature space are separated by linear *decision boundaries*, as shown by the straight lines in Figure 24. An unknown target (shown as the diamond in the figure) can be classified into a UXO of pre-determined class depending into which feature-space region fall the parameters inverted from its EMI response. The development of such a UXO classification scheme, based on neural networks, remains work in progress at Texas A&M University.

Task 3. Integrated System Tests

This section of the report describes results of testing the UX-1312 multi-receiver EMI prototype system at the Texas A&M Riverside campus field site. The field testing of the system shows promising indications that the prototype system shall be a useful instrument for its stated design purpose: buried UXO target discrimination and classification aimed at maintaining high detection probability with low false alarm rate.

Figure 25a shows the transmitter coil and nine receiver coils mounted on its wheeled chassis. The frame and wheels are made of strong, lightweight composites (plexiglass®, Lexan®, Nylon®) with zero metal content. The handle is made of wood. The receiver coils, which are numbered according to the scheme shown in Figure 25b, are connected to the receiver circuitry by shielded cables. The shield serves as a common ground and connects to the body of the aluminum circuit body. Plug connectors are implemented for each electrical connection for convenient removal, system calibration, and maintenance of each receiver coil, as needed.

Figure 26 shows the complete one-man-portable EMI system prototype as it would be deployed in a “cued sensing” mode at an actual UXO site, with the exception that the lead-acid 12-volt battery seen on the ground would be replaced by a lighter weight lithium-ion battery that is carried by the operator in a backpack.

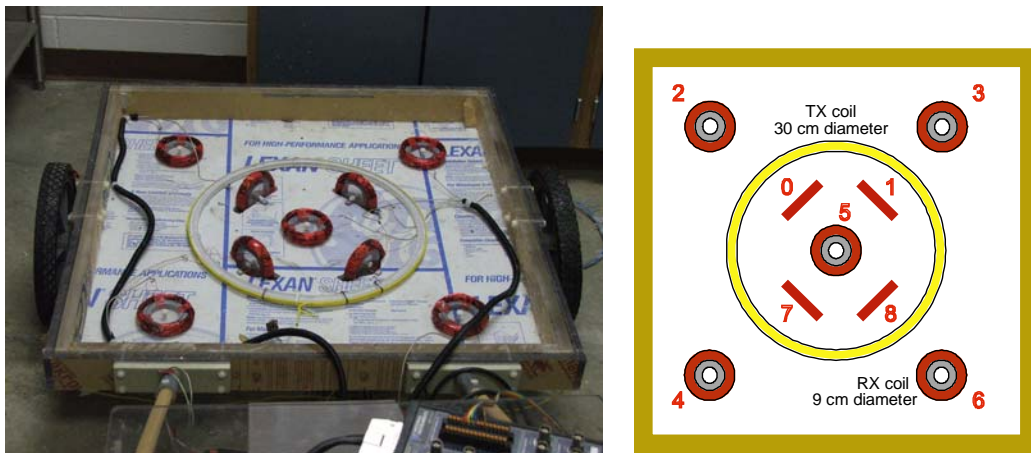


Figure 25. (a, left) Transmitter coil (large loop) and receiver coils (small loop). (b, right) Numbering scheme of the receiver coils.



Figure 26. Complete one-man-portable EMI system prototype.

Figure 27 shows typical transient EMI responses acquired at the Riverside campus test site by the central coil (number 5) of the multi-receiver UX-1312 system, with and without a UXO target present. Notice that the EMI response with UXO present, shown at the left, is clearly distinguished from the background response, shown at the right.

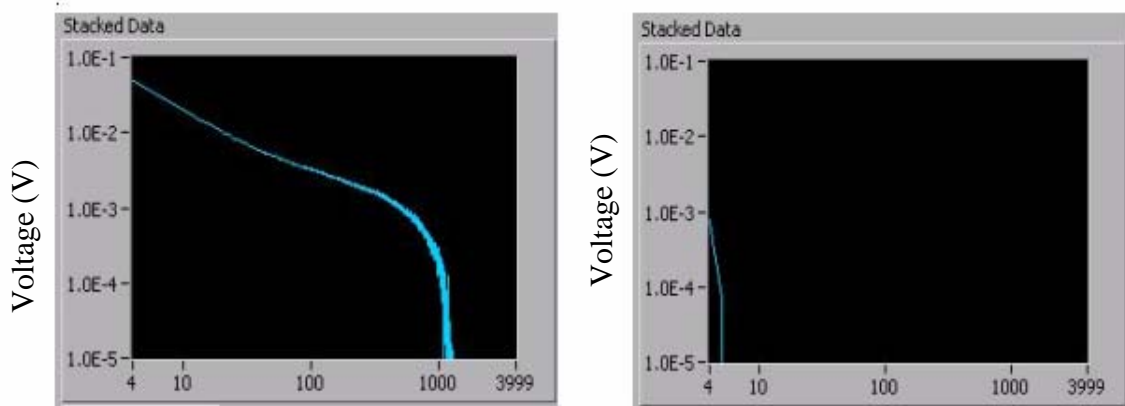


Figure 27. Riverside field test: measured responses ($5 \mu\text{s}/\text{sample}$) at the central coil receiver: (a, left) with UXO target, and (b, right) without target.

The raw EMI transient response at each receiver coil is acquired as a voltage signal sampled at 8000 points between $250 \mu\text{s}$ and 40.25 ms following the TX switch-off. The raw transients are pre-processed by integrating the raw voltage signal over the 24 pre-determined time gates shown in Table 1, below. This is done in order to increase the signal-to-noise ratio and to greatly reduce the amount of required computer storage for each EMI transient.

Table 1. Integration time gates defined for the UX-1312 multi-receiver system.

ch start	ch end	width[μ s]	avg[μ s]	start[μ s]	end[μ s]
0	12	60	280	250	310
10	25	75	337.5	300	375
22	38	80	400	360	440
36	56	100	480	430	530
66	80	70	615	580	650
78	108	150	715	640	790
106	148	210	885	780	990
144	174	150	1045	970	1120
217	255	190	1430	1335	1525
293	333	200	1815	1715	1915
331	432	505	2157.5	1905	2410
429	561	660	2725	2395	3055
556	722	830	3445	3030	3860
716	929	1065	4362.5	3830	4895
923	1191	1340	5535	4865	6205
1185	1528	1715	7032.5	6175	7890
1506	1938	2160	8860	7780	9940
1833	2357	2620	10725	9415	12035
2258	2903	3225	13152.5	11540	14765
2792	3587	3975	16197.5	14210	18185
3468	4451	4915	20047.5	17590	22505
4337	5566	6150	25010	21935	28085
5452	6996	7720	31370	27510	35230
6870	7999	5645	37422.5	34600	40245

The effect of pre-processing an 8000-point raw EMI transient prior to its storage as a 24-point time-integrated signal is shown in Figure 28. The target in this case is a 57mm anti-tank round from the standard U.S. Army inert UXO kit buried at 0.2 m directly below the central coil, RX5. The continuous lines correspond to positive voltage values while the discontinuous lines correspond to negative voltage values. The first sample point is highly variable in most of the tests, as shown typically here, and can be removed by increasing the delay between TX ramp-off trigger and the start of the acquisition. The sampling rate for this test is 200 kS/s (kS=kilosamples), the delay is 250 μ s, and the sampling interval is 5 μ s. The time-integrated signal, shown in red, provides a good indication of the raw EMI transient response but requires 99.7% less data storage.

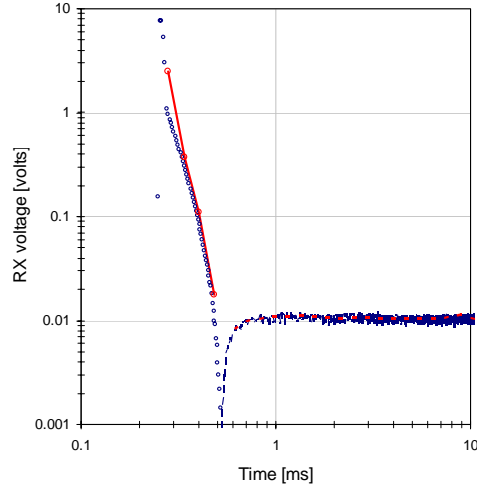


Figure 28. Raw (blue) and time-integrated (red) EMI transient from UX-1312 RX5 (at the center of the array).

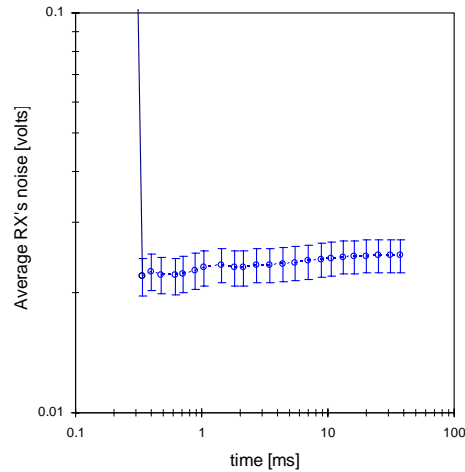


Figure 29. Results of noise test.

A test of the inherent system noise, with the TX turned off, has also been carried out at the Riverside campus test site. The results are shown in Figure 29. In this test, a total of 107 time-integrated EMI transient responses acquired by central receiver RX5 were stacked, or averaged, in the absence of any UXO target buried in the ground. The resulting signal provides an indication of the background response, which is essentially the environmental noise level. The stacked background signal level is about 20 mV, as shown in the figure. The signal level is constant over the entire signal acquisition interval, up to 100 ms.

In testing a multi-receiver system it is essential to demonstrate that the various receiver coils do not generate an excessive coupling, caused by mutual inductance of pairs of coils, that distorts or interferes with the EMI signal originating from induced currents in the buried UXO target. We have tested the mutual coupling of receiver coils within the UX-

1312 prototype array using the central receiver coil RX5 as the reference coil and vertical receiver coils RX0, RX1, RX7 and RX8 (for coil configuration, see Figure 25b) as test coils. The target is the 57mm anti-tank round buried at 0.2 m directly below RX5. Any coil in the UX-1312 system can be in one of three states: (i) absent: unplugged from the multiplexer and completely removed from the system; (ii) inactive: unplugged but remaining in its place within the RX array; (iii) active: plugged into the multiplexer and providing data.

The results of a mutual coupling test between coils RX0 and RX5 is shown in Figure 30. The RX5 EMI transient response without any other coil present in the array (*none*) is shown as the blue curve. The EMI response at RX5 with the RX0 in its place, plugged into the multiplexer (*on, active*) is shown as the green curve. Finally, the EMI response at RX5 with the RX0 coil in place but unplugged (*off, inactive*) is shown as the red curve. These are raw data plots, not time-integrated. The responses from 10-40 ms after TX switch-off are not shown. Notice that the three response curves are almost identical which indicates that the mutual coupling between the two coils RX0 and RX5 is negligible and independent of whether the coils are plugged into the multiplexer and acquiring data.

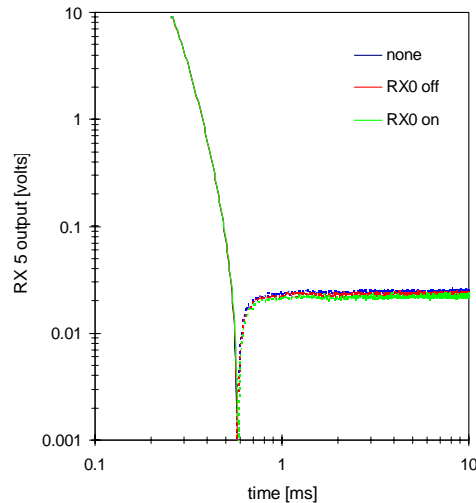


Figure 30. Simple mutual coupling test, RX0 and RX5

A more advanced mutual coupling test was next performed. In this test, the four vertical receivers RX0, RX1, RX7 and RX8 located inside the TX loop were used as the test coils. Various combinations of them were activated and inactivated and mutual coupling assessments were made. The nomenclature shown in Table 2 has been used. The results of the advanced mutual coupling test are shown in Figure 31. It is readily seen that the distribution of active/inactive RX coils does not appreciable affect the early-time EMI transient response from the buried UXO target. There is some effect on the late-time signal level. This small DC bias signal can be accounted for by a careful system calibration prior to deployment. In general, however, the mutual coupling tests have indicated that the effect of mutual inductance of pairs of RX coils is not a critical factor in shaping the overall UX-1312 system performance.

Table 2. Nomenclature for advanced mutual coupling test.

Response	RX5	RX0	RX1	RX7	RX8
5-0178	active	inactive	inactive	inactive	inactive
5-0c178	active	active	inactive	inactive	inactive
5-0c1c78	active	active	active	inactive	inactive
5-0c1c7c8	active	active	active	active	inactive
5-0c1c7c8c	active	active	active	active	active

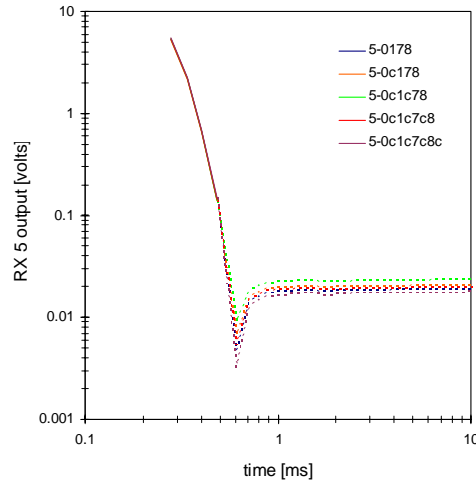


Figure 31. Advanced mutual coupling test, RX0, RX1, RX7, RX8 and RX5

The final field test was conducted to examine the performance of the entire RX array on a buried metal target. Stacked transients ($N=100$) for the various receiver coils in the presence of a 3-inch steel disk, and a 6-inch aluminum disk are shown in Figure 32. The compressed transients are shown in the top panel, for ease of plotting, as $\text{sgn}(V)\sqrt{|V|}$ where V is the measured RX voltage. The equivalent background-subtracted compressed transients, defined as the difference of the measured RX voltage with and without target present, are shown in the bottom panel. It is evident that the UX-1312 instrument can distinguish the two targets once the background signal is removed. Again, a rigorous system calibration is clearly required before the system is field-deployable.

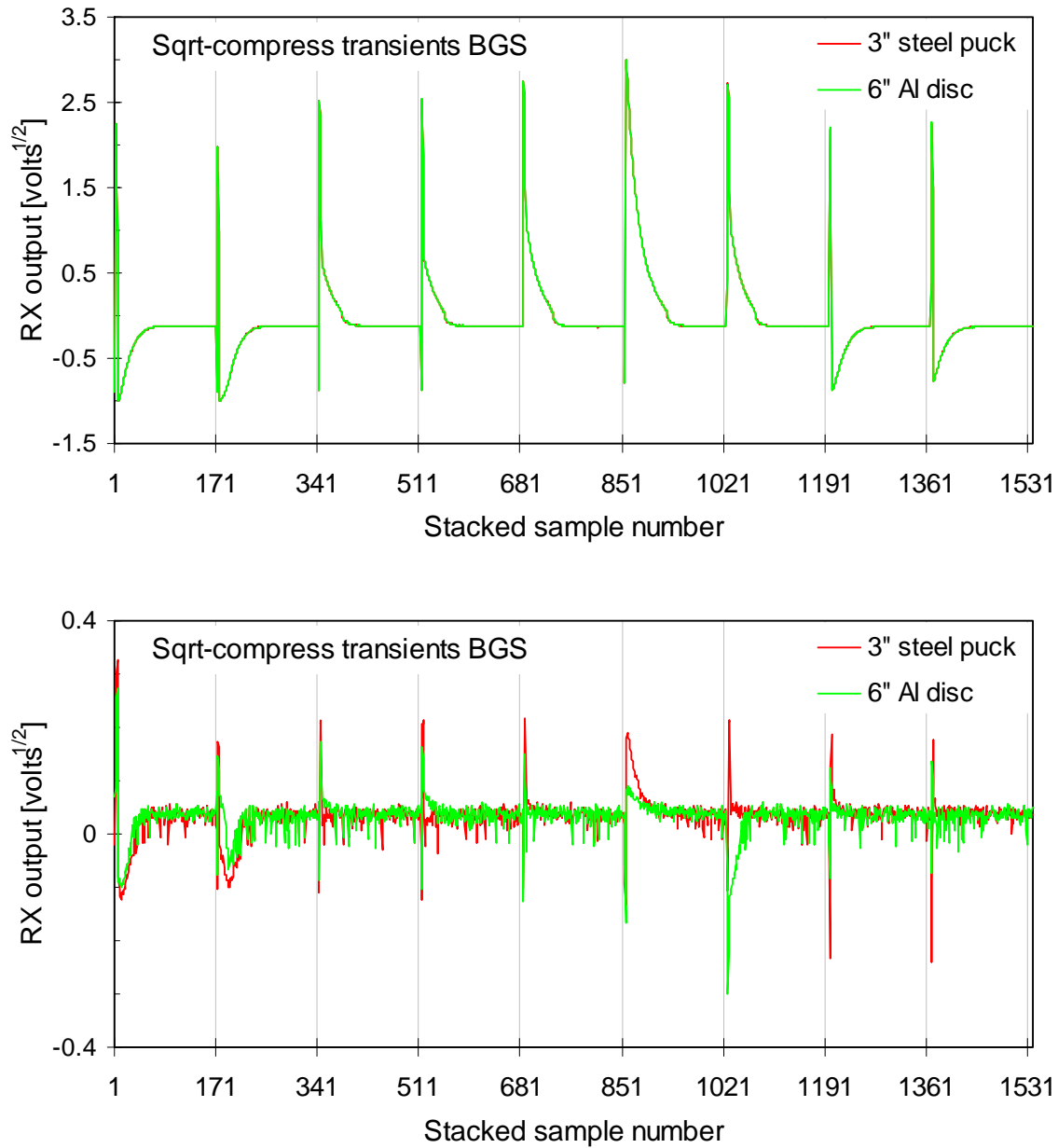


Figure 32. Stacked EMI transients for the entire 9-RX array. The signals in the bottom panel are background-subtracted. The transients are shown sequentially from left as: RX8, RX1, RX3, RX6, RX4, RX5 (central loop), RX2, RX0, RX7.

Conclusions

Unexploded ordnance (UXO) detection, discrimination and removal represents a priority environmental problem at U.S. military bases facing closure and realignment and many other regions of the world. Despite recent advances in geophysical technologies and signal processing algorithms the false alarm rates remain unacceptably high. The SERDP project UX-1312 responded to the challenge to develop improved electromagnetic

induction (EMI) sensors and algorithms capable of recording target responses, isolating them from geological noise, and processing them to discriminate the nature of the target.

A multi-sensor EMI system prototype has been developed. The system consists of a transmitter, a multi-channel receiver, a power supply module, a transmitting coil, multiple receiving coils, and a signal processing unit. The transmitter, receiver and power supply constitute the system's main hardware and are completely designed on a single circuit board, thus making the system very compact and man-portable. The developed system has been demonstrated in laboratory and field for detection of UXO.

EMI interpretation software has been developed to discriminate UXO from non-UXO such as clutter or exploded metal fragments and, furthermore, to classify UXO into various categories such as mortars, artillery shells, submunitions, etc. The UXO/clutter/fragment discrimination and UXO classification rests on an interpretation of the EMI transients in terms of target parameters such as location, depth, orientation, shape, electrical conductivity and magnetic permeability. The EMI interpretation is cast as a parametric nonlinear inverse problem. The discrimination and classification algorithms are treated as pattern recognition tasks.

The UX-1312 multi-receiver EMI prototype system was tested at the Texas A&M Riverside campus field site and shows promising indications that the prototype system shall be a useful instrument for its stated design purpose. A rigorous system calibration is required before the system can be confidently deployed in the field.

UX1312-related publications

Benavides, A., Everett, M.E., Pierce, C. and Nguyen, C 2003. Fractal properties of background noise and target signal enhancement using CSEM data, *Proc. SPIE 5089: Detection and Remediation Technologies for Mines and Mine-like Targets VIII.*, Orlando FL, p 807-817.

Benavides, A. and Everett, M.E. 2005. Target signal detection in near-surface controlled-source electromagnetic induction data, *Geophysics* **70**, G59-G67

Benavides, A. and Everett, M.E. 2006. Nonlinear inversion of controlled-source multi-receiver electromagnetic induction data for unexploded ordnance using a continuation method, *J Applied Geophysics* (paper under review)

Everett, M.E. 2004. An experimental study of the transient electromagnetic response of connected conductor networks (abstract GP14A-05), *Eos* **85**, Fall 2004 Fall AGU Meeting Supplement

Everett, M. E., Benavides, A. and Pierce, C. J., 2005. An experimental study of the time-domain electromagnetic response of a buried conductive plate. *Geophysics*, **70**, p. G1-G7. 10.1190/1.1852773.

Everett, M.E. 2005. What do electromagnetic induction responses measure? *The Leading Edge* **24**, 154-157.

Everett, M.E., Benavides, A., and Nguyen, C.V. 2005. Challenges to near-real time classification of buried conductive targets based on spatiotemporal EMI responses (abstract NS12A-01, invited), *Eos* **86**, 2000 AGU/SEG Joint Assembly

Guan, X., Jin, Y., Nguyen, C. and Everett, M.E. 2004. Multi-sensor EMI system prototypes for UXO detection and classification *Proc. UXO/Countermine Forum*, St Louis MO, 6 pp.

Stalnaker, J., Everett, M.E., Benavides, A. and Pierce, C. 2005. Mutual inductance and the effect of host conductivity on EM induction response of buried plate targets using 3-D finite element analysis, *IEEE Trans Geosci Remote Sensing* **44**, 251-259.

References

- Ao, C. O., Braunisch, H., O'Neill, K. and Kong, J. A., 2002. Quasi-Magnetic solution for a conducting and permeable spheroid with arbitrary excitation. *IEEE Trans. Geosci. Rem. Sens* **40**, 4, p. 887-897. S 0196-2892(02)04590-4.
- Bube, K. P., and Langan, R. T., 1990. On a continuation approach to regularization for crosswell tomography: 69th Ann. Internat. Mtg., Soc. Explor. Geophys., Expanded Abstracts, bf 2.
- Burrows, M. L., A theory of eddy current flaw detection. Ph.D. thesis, University of Michigan, Ann Harbor, 1964.
- Chamberlin, R. V., Mozurkewich, G. and Orbach, R., 1984. Time delay of the remanent magnetization in spin-glasses. *Phys. Rev. Lett.*, **52**, 10, p. 867-870.
- Das, Y., McFee, J. E., Toews, J., and Stuart, G. C., 1990. Analysis of an electromagnetic induction detector for real-time location of buried objects. *IEEE Trans. on Geosci. Remote Sensing* **28**, 3, p. 278-287.
- De Villiers, N. and Glasser, D., 1981. A continuation method for nonlinear regression. *SIAM J. Numer. Anal.*, **18**, 1139-1154.
- Everett, M. E. 1996. Homotopy, polynomial equations, gross boundary data, and small Helmholtz systems. *J. Comput. Phys.*, **124**, 431-441.
- Everett, M. E., Benavides, A. and Pierce, C. J., 2005. An experimental study of the time-domain electromagnetic response of a buried conductive plate. *Geophysics*, **70**, p. G1-G7. 10.1190/1.1852773.
- Garcia, C. B. and Zangwill, W. I., 1981. *Pathways to Solutions, fixed points and equilibria*: Prentice Hall, Inc.
- Geonics Limited, 2002. EM63 Full time domain electromagnetic UXO detector. Operating instructions.
- Jegen, M. D., Everett, M. E. and Schultz, A., 2001. Using homotopy to invert geophysical data. *Geophysics*, **66**, 1749-1760.
- Keller, H. B., and Perozzi, D. J., 1983. Fast seismic ray tracing. *SIAM J. Appl. Math.*, **43**, 981-992.
- Laherrere, J. and Sornette, D., 1998. Stretched exponential distributions in nature and economy: "fat tails" with characteristic scales. *Eur. Phys. J. B*, **2**, 525-539.
- Madsen, K., Nielsen, H. B., Tingleff, O., 2004. Methods for non-linear least squares problems. IMM, DTU report IMM-REP-2004-01. Technical University of Denmark.
- Mrozynsky, G., 1998. Analytical determination of Eddy currents in a hollow sphere excited by an arbitrary dipole. *IEEE Trans. Mag.*, **34**, 3822-3829. S0018-9464(98)06717-X.
- Nocedal, J. and Wright, S. J., 1999. *Numerical Optimization*. Springer Series in Operations Research. Springer-Verlag, New York.

- Pasion, L.R. and Oldengurg, D. W., 2001. Locating and characterizing unexploded ordnance using time domain electromagnetic induction. Geotechnical and Structures Laboratory, ERDC/GSL TR-01-10. US Army Corps of Engineers, 82p.
- Rheinboldt, W. C., 1980. Solution fields of nonlinear equation and continuation methods. SIAM J. Numer. Anal., 17, 221-237.
- Vasco, D. W., 1994. Singularity and branching: A path following formalism for geophysical inverse problems. Geophys. J. Internat., 19, 809-830.
- Vasco, D. W., 1998. Regularization and trade-off associated with nonlinear geophysical inverse problems: penalty homotopies. Inverse Problems, 14, 1033-1052.
- Watson, L. T., 1989. Globally convergent homotopy methods: a tutorial. Appl. Math. Comp., 31, 369-396.
- Williams, G. and Watts, D. C., 1970. Trans. Faraday Soc., 66, 80.
- Zhang, Y., Collins, L., and Carin, L., 2003. Physics model based unexploded ordnance discrimination using wideband EMI data, Proceedings of SPIE. Detection and remediation technologies for mines and minelike targets VIII, vol. 5089. p. 1023-1045.